A non-intrusive reduced basis method using artificial neural networks

J.S. Hesthaven, S. Ubbiali

École Polytechnique Fédérale de Lausanne (EPFL), CH-1015 Lausanne, Switzerland

Abstract

In this work, we develop a non-intrusive reduced basis (RB) method for parametrized time-indepedent partial differential equations (PDEs). The proposed method extracts a reduced basis from a collection of high-fidelity solutions via proper orthogonal decomposition (POD) and employs artificial neural networks (ANNs), particularly multi-layer perceptrons (MLPs), to accurately approximate the coefficients of the reduced model. The search for the optimal number of inner neurons and the minimum amount of training samples which avoids overfitting is carried out in the offline phase through an automatic routine, relying upon a joint use of the latin hypercube sampling (LHS) and the Levenberg-Marquardt training algorithm. This guarantees a complete offline-online decoupling, leading to an efficient RB method - referred to as POD-NN - suitable also for nonlinear problems featuring a non-affine parametric dependence. Numerical studies are presented for the nonlinear Poisson equation and for driven cavity viscous flows, modeled through the steady uncompressible Navier-Stokes equations. Both physical and geometrical parametrizations are considered. Several results confirm the accuracy of the POD-NN method and show the substantial speed-up enabled at the online stage with respect to a traditional RB strategy based on the Galerkin projection process.

Keywords: non-intrusive reduced basis method, proper orthogonal decomposition, multi-layer perceptron, Levenberg-Marquardt algorithm, Poisson equation, driven cavity flow

1. Introduction

Several applications arising in engineering and applied sciences involve mathematical models expressed as parametrized partial differential equations (PDEs), in which boundary conditions, material properties, source terms, loads or geometrical factors of the underlying physical problem are addressed to a parameter $\boldsymbol{\mu}$ [19, 30, 34]. A list of notable examples includes parameter estimation [6], topology optimization [5], optimal control [40] and uncertainty quantification [39]. In these contexts, one is typically interested in a real-time evaluation of an *output of interest* (defined as a functional of the state variable [16]) for many parameter entries, i.e., for many configurations of the problem.

The continuously growing availability of computational power and the simultaneous algorithmic improvements make possible nowadays the *high-fidelity* numerical resolution of complex problems via standard discretization procedures, such as finite difference (FD), finite volume (FV), finite element (FE), or spectral methods [53]. However, these schemes remain prohibitevely expensive in many-query and real-time contexts, both in terms of CPU time and memory demand. This follows from the large amount of degrees of freedom (DOFs) they imply, resulting from the (fine) spatial discretization needed to accurately solve the underpinning PDE [1]. In light of this, *reduced order modeling* (ROM) methods have received a significant attention in the last decades. The objective of these methods is to replace the full-order system by one of significant smaller dimension, thus to decrease the computational burden while leading to a reasonable loss of accuracy [12].

Reduced basis (RB) methods constitute a well-known and widely-used instance of reduced order modeling techniques. They are generally implemented pursuing an offline-online paradigm [41]. Based upon an ensemble of *snapshots* (i.e., high-fidelity solutions to the parametrized differential problem), the goal of the *offline* step is to construct a solution-dependent basis, yielding a reduced space of globally approximating functions capable of representing the main dynamics of the full-order model [2, 12]. For this, two major approaches have been proposed in the literature: proper orthogonal

Email addresses: `jan.hesthaven@epfl.ch` (J.S. Hesthaven), `stefano.ubbiali@epfl.ch` (S. Ubbiali)

decomposition (POD) [60] and greedy algorithms [31]. The former relies on a deterministic or random sample to generate the snapshots and then employs a singular value decomposition (SVD) to recover the reduced basis. Whereas, the latter adopt a different strategy, as the basis vectors coincide with the snapshots themselves, carefully selected according to some optimality criterion. As a result, a greedy strategy is typically more effective and efficient than POD, as it enables the exploration of a wider region of the parameter space while entailing the computation of many fewer high-fidelity solutions [30]. However, there may exist problems for which a greedy approach is not feasible, simply because a natural criterion for the choice of the snapshots is not available [2].

When a reduced-order environment has been properly set up, given a new parameter input, an approximation to the *truth* solution is sought *online* as a linear combination of the RB functions. The expansion coefficients are determined via projection of the full-order system onto the reduced space [7]. To this end, a Galerkin procedure is the most popular choice.

Despite their established effectiveness, for complex nonlinear problems with a non-affine dependence on the parameters, projection-based RB methods do not provide any computational gain with respect to a direct (expensive) approach, as the cost to compute the projection coefficients depends on the dimension of the full-order model. In fact, a full decoupling between the online stage and the high-fidelity scheme is the ultimate secret for the success of any RB procedure [53]. For this purpose, one may recover an affine expansion of the differential operator through the empirical interpolation method (EIM) [3] or its discrete variants [10, 49].

A valuable alternative to address this concern is represented by *non-intrusive* RB methods, which refer to the high-fidelity model solely to generate the snapshots, without involving it in the projection process [12]. The projection coefficients are then obtained via interpolation over the parameter domain of a database of reduced-order information [9]. However, it should be noted that reduced bases generally belong to nonlinear, matrix manifolds. Hence, unless using a large amount of samples, standard interpolation techniques may fail, as they cannot enforce the constraints characterizing those manifolds [1, 4].

In this work, we develop a non-intrusive RB method employing POD for the generation of the reduced basis and resorting to (artificial) neural networks, in particular multi-layer perceptrons, in the interpolation step. Hence, in the following we refer to the proposed RB procedure as the POD-NN method. Being of non-intrusive nature, POD-NN is suitable for a fast and reliable resolution of complex nonlinear PDEs featuring a non-affine parametric dependence. To test its accuracy and efficiency, the POD-NN method is applied to the nonlinear Poisson equation and to the steady uncompressible Navier-Stokes equations. Both physical and geometrical parametrizations are considered.

The paper is organized as follows. Section 2 discusses components, topology and learning process of the artificial neural networks used in the simulations. In particular, Subsection 2.3.1 outlines the Levenberg-Marquardt training algorithm. Section 3 defines the (parametrized) functional and variational framework which is required to develop a finite element solver, briefly described in Section 4. The standard projection-based POD-Galerkin (POD-G) RB method is derived in Section 5, while the proposed non-intrusive POD-NN RB procedure is detailed in Section 6; both theoretical and practical aspects are addressed. Several numerical results, aiming to show the reliability and efficiency of the proposed RB technique, are offered in Section 7 for the Poisson equation (Subsections 7.1 and 7.2) and the lid-driven cavity problem for the steady Navier-Stokes equations (Subsection 7.3). Finally, Section 8 gathers some relevant conclusions and suggests future developments.

2. Artifical neural networks

Inspired by the biological information processing system (see, e.g., [26, 38]), an *artificial neural network* (ANN), usually simply referred to as *neural network*, is a computational model capable to learn from observational data, i.e., by example, thus providing an alternative to the algorithmic programming paradigm [48]. As its original counterpart, it consists of a collection of processing units, called (artificial) *neurons*, and directed *weighted synaptic* connections among the neurons. Data travel among neurons through the connections, following the direction imposed by the synapses. Hence, an artificial neural network is an *oriented graph* to all intents and purposes, with the neurons as *nodes* and the synapses as oriented *edges*, whose weights are adjusted by means of a *training* process to configure the network for a specific application [59].

Formally, a neural network could be defined as follows [38].

Definition 2.1 (Neural network). *A* neural network *is a sorted triple* $(\mathcal{N}, \mathcal{V}, w)$*, where* $\mathcal{N}$ *is the set of* neurons*, with cardinality* $|\mathcal{N}|$, $\mathcal{V} = \{(i, j), 1 \leq i, j \leq |\mathcal{N}|\}$ *is the set of* connections*, with* (i, j) *denoting the oriented connection linking the sending neuron* i *with the target neuron* j*, and* $w : \mathcal{V} \to \mathbb{R}$ *is the* weight function*, defining the weight* $w_{i,j} = w((i, j))$

of the connection (i,j). A weight may be either positive or negative, making the underlying connection either excitatory or inhibitory, respectively. By convention, $w_{i,j} = 0$ means that neurons i and j are not directly connected.

In the following, we dive deeper into the structure and training of a neural network, starting by detailing the structure of an artificial neuron.

2.1. Neuronal model

An artificial neuron represents a simplified model of a biological neuron [38]. To introduce the components of the model, let us consider the neuron j represented on the left in Fig. 2.1. Suppose that it is connected with m sending neurons $\{s_1,\dots,s_m\}$, and n receiving (target) neurons $\{r_1,\dots,r_n\}$. Denoting by $y_\Omega(t) \in \mathbb{R}$ the scalar output fired by a generic neuron Ω at time t, neuron j gets the weighted inputs $w_{s_k,j}\, y_{s_k}(t)$, $k = 1,\dots,m$, at time t, and sends out the output $y_j(t+\Delta t)$ to the target neurons $\{r_1,\dots,r_n\}$ at time $t+\Delta t$. In particular, neuron r_i, $i = 1,\dots,n$, receives as input $w_{j,r_i}\, y_j(t+\Delta t)$. Please note that in the context of ANNs the time is discretized by introducing the timestep Δt. This is clearly not plausible from a biological viewpoint; however, it substantially simplifies the implementation. In the following, we will avoid to specify the dependence on time unless strictly necessary, thus to lighten the notation.

An artificial neuron j is completely characterized by three functions: the propagation function, the activation function, and the output function. These will be defined and detailed below in the same order they get involved in the data flow.

Propagation function. The propagation function f_{prop} converts the vectorial input $\mathbf{p} = [y_{s_1},\dots,y_{s_m}]^T \in \mathbb{R}^m$ into a scalar u_j often called *net input*, i.e.,

$$u_j = f_{prop}(w_{s_1,j},\dots,w_{s_m,j}, y_{s_1},\dots,y_{s_m})\,.$$

A common choice for f_{prop} (used also in this work) is the weighted sum, adding up the scalar inputs multiplied by their respective weights:

$$f_{prop}(w_{s_1,j},\dots,w_{s_m,j}, y_{s_1},\dots,y_{s_m}) = \sum_{k=1}^{m} w_{s_k,j}\, y_{s_k}\,. \tag{2.1}$$

The function (2.1) provides a simple, yet effective way of modeling the accumulation of different input electric signals within a biological neuron [26].

Activation or transfer function. At each timestep, the *activation state a_j*, often referred to as *activation*, quantifies to which extent neuron j is currently active or excited. It results from the activation function f_{act}, which combines the net input u_j with a threshold $\theta_j \in \mathbb{R}$ [38]:

$$a_j = f_{act}(u_j;\theta_j) = f_{act}\big(\sum_{k=1}^{m} w_{s_k,j}\, y_{s_k};\theta_j\big)\,,$$

where we have employed the weighted sum (2.1) as propagation function. Note that the threshold θ_j is a parameter of the network and as such one may choose to adapt it through a training process, exactly as it can be done for the synaptic weights. To ease the runtime access of θ_j, it is common practice to introduce a *bias neuron* in the network. A bias neuron is a continuously firing neuron, with constant output $y_b = 1$, which is directly connected with neuron j, assigning the *bias weight* $w_{b,j} = -\theta_j$ to the connection. As can be deduced by the representation on the right in Fig. 2.1, θ_j is now treated as a synaptic weight, while the neuron threshold is set to zero. Hence, the net input becomes

$$u_j = \sum_{k=1}^{m} w_{s_k,j}\, y_{s_k} - \theta_j\,,$$

i.e., the threshold is included in the propagation function rather than in the activation function, which we can now express in the form

$$a_j = f_{act}\big(\sum_{k=1}^{m} w_{s_k,j}\, y_{s_k} - \theta_j\big)\,.$$

Conversely to the propagation function, there exist various choices for the activation function. Sigmoid functions have been widely used for the realization of artificial neural networks due to their graceful combination of linear and nonlinear behaviour [26]. Sigmoid functions are s-shaped, monotically increasing, and assume values in a bounded interval. A

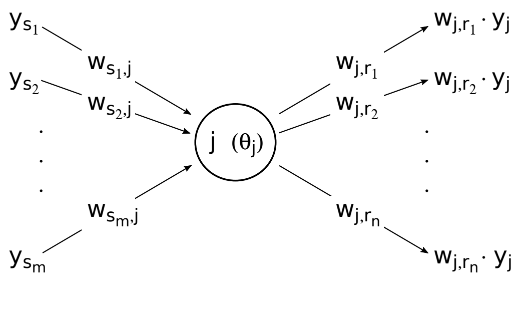

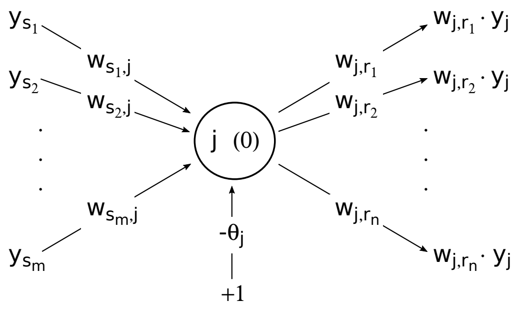

Figure 2.1. Visualization of the generic j-th neuron of an artificial neural network, including (right) or not (left) a bias neuron. On the left, the neuron accumulates the weighted inputs $\{w_{s_1,j}\ y_{s_1}, \dots, w_{s_m,j}\ y_{s_m}\}$ respectively coming from the sending neurons $s_1, \dots, s_m$; on the right, the neuron accumulates the weighted inputs $\{w_{s_1,j}\ y_{s_1}, \dots, w_{s_m,j}\ y_{s_m}, -\theta_j\}$ respectively coming from the sending neurons $s_1, \dots, s_m$, b, with b the bias neuron. In both situations, the neuron then fires y_j, sent to the target neurons $\{r_1, \dots, r_n\}$ through the synapsis $\{w_{j,r_1}, \dots, w_{j,r_n}\}$. The neuron threshold is reported in brackets within its body.

well-known instance is given by the hyperbolic tangent,

$$f_{act}(v) = \frac{e^{v} - e^{-v}}{e^{v} + e^{-v}}\,.$$

Output function. Finally, the output function f_{out} calculates the scalar *output* $y_j \in \mathbb{R}$ based on the activation state a_j of the neuron:

$$y_j = f_{out}(a_j)\,.$$

Typically, f_{out} is the identity function, so that activation and output of a neuron coincides, i.e., $y_j = f_{out}(a_j) = a_j$. Note that while the input $\mathbf{p} = [y_{s_1}, \dots, y_{s_m}]^T \in \mathbb{R}^m$ of the neuron is generally vectorial, i.e., $m > 1$, the output is scalar. The output y_j could then be sent either to other neurons or constitute a component of the overall output vector of the network, as for the neurons in the output layer of a feedforward neural network, illustrated in the following subsection.

The neural model presented so far refers to the so called *computing* neuron, i.e., a neuron which process input information to provide a response. However, in a neural network one may also identify *source* neurons, supplying the network with the respective components of the activation pattern (input vector), without performing any computation [26].

2.2. Network topology: the feedforward neural network

The way neurons are interconnected within a network defines the *topology* of the network itself, i.e., its design. In the literature, many network architectures have been proposed, sometimes tailored to a specific application. Among all, *feedforward neural networks*, also called *perceptrons* [56], have been typically preferred in function regression tasks.

In a feedforward neural network, neurons are arranged into *layers*, with one *input layer* of M_I source neurons, K *hidden layers*, each one consisting of H_k computing neurons, $k = 1, \dots, K$, and an *output layer* of M_O computing neurons. As a characteristic property, neurons in a layer can only be connected with neurons in the next layer towards the output layer, and not within the same layer. Then, an *activation pattern* $\mathbf{p} \in \mathbb{R}^{M_I}$, supplied to the network through the source nodes in the first layer, provides the input signal for the neurons in the first hidden layer. For each hidden layer, its output signals give the input pattern for the following layer. In this way, information travels towards the last layer of the network, i.e., the output layer, whose outputs constitute the components of the overall output $\mathbf{q} \in \mathbb{R}^{M_O}$ of the network [1]. Hence, a feedforward network establishes a map between the *input space* $\mathbb{R}^{M_I}$ and the *output space* $\mathbb{R}^{M_O}$. This makes this network architecture particularly suitable for continuous function approximation.

[1] Please note that while the output of a single neuron is denoted with the letter y, we use the letter $\mathbf{q}$ (bolded) to indicate the overall output of the network. Clearly, for the j-th output neuron the output y_j coincides with the corresponding entry of $\mathbf{q}$, i.e., $q_j = y_j$, $j = 1, \dots, M_O$.

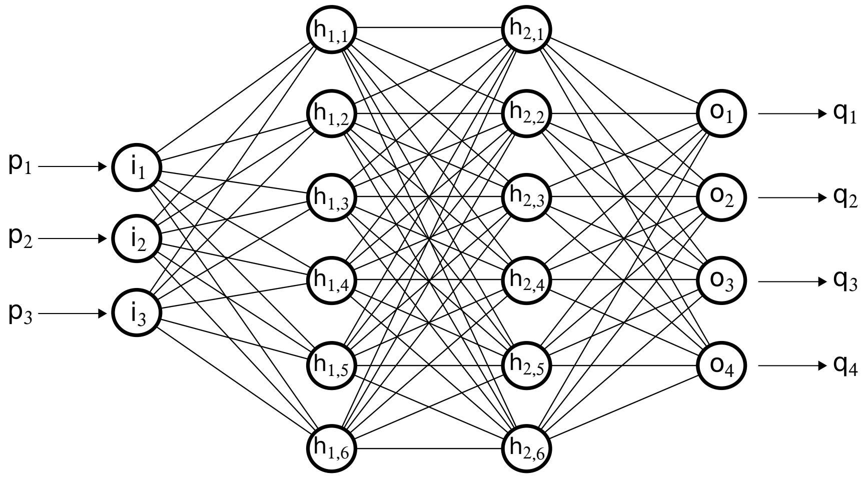

Figure 2.2. A three-layer feedforward neural network, with 3 input neurons, two hidden layers each one consisting of 6 neurons, and 4 output neurons. Within each connection, information flows from left to right.

Feedforward networks can be classified according to the number of hidden layers or, equivalently, the number of layers of trainable weights. Single-layer perceptrons (SLPs) consist of the input and output layer, without any hidden layer. Because of their quite simple structure, the range of application of SLPs is rather limited. Indeed, only *linearly separable* data can be properly represented using SLPs [38]. Conversely, multi-layer perceptrons (MLPs), with at least one hidden layer, are universal function approximators, as stated by Cybenko [13, 14]. In detail:

(i) an MLP with one layer of *hidden neurons* and differentiable activation functions can approximate any *continuous* function [14];

(ii) an MLP with two layers of *hidden neurons* and differentiable activation functions can approximate *any function* [13].

Therefore, in many practical applications there is no reason to employ MLPs with more than two hidden layers. However, (i) and (ii) do not give any practical advice neither on the number of hidden neurons nor the number of samples required to train the network: these should be found pursuing a *trial-and-error* (and likely time-consuming) approach [24].

An instance of a three-layer (i.e., two hidden layer plus the output layer) feedforward network is offered in Fig. 2.2. In this case, we have $M_I = 3$ input neurons (denoted with the letter i), $H_1 = H_2 = 6$ hidden neurons (letter h for both hidden layers), and $M_O = 4$ output neurons (letter o). In particular, it represents an instance of a *completely linked* perceptron, since each neuron is directly connected with all neurons in the following layer.

2.3. Training a multi-layer feedforward neural network

As previously mentioned, the principal characteristic of a neural network is its capability of *learning* from the surrounding environment by storing the acquired knowledge via the network internal parameters, i.e., the synaptic and bias weights. Learning is accomplished through a training process, during which the network is exposed to a collection of examples, called *training patterns*. According to some performance measure, the weights are then adjusted by means of a well-defined set of rules. Therefore, the learning procedure is an *algorithm*, typically iterative, such that after a successfull training, the neural network provides reasonable responses for unknown problems of the same class of the training set. This property is known as *generalization* [38].

Training algorithms can be classified based on the nature of the training set, i.e., the set of training patterns. We can then distinguish three *learning paradigms*: supervised learning, unsupervised learning and reinforcement learning [24]. The choice of the learning paradigm is task-dependent. In particular, for function approximation, the *supervised* learning paradigm is the best choice.

Consider the nonlinear unknown function $\boldsymbol{f}$,

$$\begin{aligned} \boldsymbol{f} \,:\, & \mathbb{R}^{M_I} \to \mathbb{R}^{M_O} \\ & \mathbf{x} \quad \mapsto \mathbf{y} = \boldsymbol{f}(\mathbf{x}) \,, \end{aligned}$$

and a set of labeled examples $\{\mathbf{p}_i, \mathbf{t}_i = \boldsymbol{f}(\mathbf{p}_i)\}_{i=1}^{N_{tr}}$ which form the training set. Note that at each *input pattern* $\mathbf{p}_i \in \mathbb{R}^{M_I}$, $i = 1, \dots, N_{tr}$, corresponds an associated desired output or *teaching input* $\mathbf{t}_i \in \mathbb{R}^{M_O}$. The goal is to approximate $\boldsymbol{f}$ over a domain $D \subset \mathbb{R}^{M_I}$ up to a user-defined tolerance ϵ, i.e.,

$$||\boldsymbol{F}(\mathbf{x}) - \boldsymbol{f}(\mathbf{x})|| < \epsilon \quad \forall \mathbf{x} \in D \,,$$

where $\boldsymbol{F} : \mathbb{R}^{M_I} \to \mathbb{R}^{M_O}$ is the actual input-output map established by the neural network, and $||\cdot||$ is some suitable norm on $\mathbb{R}^{M_O}$. To this end, the synaptic and bias weights are iteratively adjusted according to a set of well-defined rules. Consider the synapsis between a sending neuron i and a target neuron j. At the t-th iteration (also called *epoch*) of the training procedure, the weight $w_{i,j}(t)$ of the connection (i, j) is modified by the time-dependent quantity $\Delta w_{i,j}(t)$, whose form depends on the specific learning rule. Hence, at the subsequent iteration $t+1$ the synaptic weight is simply given by

$$w_{i,j}(t+1) = w_{i,j}(t) + \Delta w_{i,j}(t) \,.$$

The whole training process is driven by an *error* or *performance* function E, which measures the discrepancy between the neural network knowledge of the surrounding environment and the actual state of the environment itself. In other terms, the bigger the output of the performance function is, the farther the neural network representation of the world is from the actual reality. Therefore, every learning rule aims to *minimize* the performance E. For this purpose, E should be a scalar function of the free parameters, i.e., the weights, of the network, namely

$$E = E(\mathbf{w}) \in \mathbb{R} \,.$$

with $\mathbf{w} \in \mathbb{R}^{|\mathcal{V}|}$ be the vector collecting the weights $\{w_{i,j} = w((i,j))\}_{(i,j) \in \mathcal{V}}$. Thus, the point over the error surface reached at the end of a successful training process provides the *optimal* configuration $\mathbf{w}_{opt}$ for the network. A common choice for the performance function is the (accumulated) mean squared error (MSE)

$$E(\mathbf{w}) = \sum_{\mathbf{p} \in P} E_{\mathbf{p}}(\mathbf{w}) = \sum_{\mathbf{p} \in P} \frac{1}{M_O} \sum_{j=1}^{M_O} \left(t_{\mathbf{p},j} - q_{\mathbf{p},j}\right)^2 \,, \tag{2.2}$$

where P is the training set, the subscript $\mathbf{p}$ refers to the input pattern, $\mathbf{t}$ is the teaching input and $\mathbf{q}$ the actual output. Note that (2.2) accounts for the error committed on each input pattern in the training set, leading to a so-called *offline* learning procedure.

In our numerical tests, at each epoch t the weight update $\Delta \mathbf{w}(t)$ is computed via the Levenberg-Marquardt algorithm, derived in the following subsection.

2.3.1. The Levenberg-Marquardt algorithm

The Levenberg-Marquardt algorithm [42] stands as an approximation to Newton's method [23]. According to the latter, at each iteration the *search direction* $\Delta \mathbf{w}$ is sought by solving the following linear system:

$$\nabla^2 E(\mathbf{w}) \; \Delta \mathbf{w} = -\nabla E(\mathbf{w}) \,, \tag{2.3}$$

where $\nabla E(\mathbf{w})$ and $\nabla^2 E(\mathbf{w})$ denotes, respectively, the gradient vector and the Hessian matrix of E with respect to its argument $\mathbf{w}$. Assume that the loss function is represented as the accumulated MSE and let us denote by $\mathbf{e}_{\mathbf{p}}$ the error vector corresponding to the input pattern $\mathbf{p}$, namely, $\mathbf{e}_{\mathbf{p}} = \mathbf{t}_{\mathbf{p}} - \mathbf{q}_{\mathbf{p}}$. Introducing the Jacobian $J_{\mathbf{p}}$ of the specific error vector $\mathbf{e}_{\mathbf{p}}$ with respect to $\mathbf{w}$, i.e.,

$$J_{\mathbf{p}}(\mathbf{w}) = \begin{bmatrix} \dfrac{\partial e_{\mathbf{p},1}}{\partial w_1} & \cdots & \dfrac{\partial e_{\mathbf{p},1}}{\partial w_{|\mathcal{V}|}} \\ \vdots & \ddots & \vdots \\ \dfrac{\partial e_{\mathbf{p},M_O}}{\partial w_1} & \cdots & \dfrac{\partial e_{\mathbf{p},M_O}}{\partial w_{|\mathcal{V}|}} \end{bmatrix} \in \mathbb{R}^{M_O \times |\mathcal{V}|}$$

simple computations yield

$$\nabla E(\mathbf{w}) = \sum_{\mathbf{p}\in P} \frac{2}{M_0} J_{\mathbf{p}}(\mathbf{w})^T \mathbf{e}_{\mathbf{p}} \in \mathbb{R}^{|\mathcal{V}|} \tag{2.4}$$

and

$$\nabla^2 E(\mathbf{w}) = \sum_{\mathbf{p}\in P} \frac{2}{M_O} \left[J_{\mathbf{p}}(\mathbf{w})^T J_{\mathbf{p}}(\mathbf{w}) + S(\mathbf{w}) \right] \in \mathbb{R}^{|\mathcal{V}|\times|\mathcal{V}|}, \tag{2.5}$$

with

$$S(\mathbf{w}) = \sum_{\mathbf{p}\in P} \frac{2}{M_O} \sum_{j=1}^{M_O} e_{\mathbf{p},j} \nabla^2 e_{\mathbf{p},j}.$$

Assuming $S(\mathbf{w}) \approx 0$, inserting (2.4) and (2.5) into (2.3) we get the linear system

$$\left[\sum_{\mathbf{p}\in P} J_{\mathbf{p}}(\mathbf{w})^T J_{\mathbf{p}}(\mathbf{w}) \right] \Delta\mathbf{w} = -\sum_{\mathbf{p}\in P} J_{\mathbf{p}}(\mathbf{w})^T \mathbf{e}_{\mathbf{p}}(\mathbf{w}). \tag{2.6}$$

The Levenberg-Marquardt modification to Newton's method reads [23, 42]:

$$\left[\sum_{\mathbf{p}\in P} J_{\mathbf{p}}(\mathbf{w})^T J_{\mathbf{p}}(\mathbf{w}) + \mu I \right] \Delta\mathbf{w} = -\sum_{\mathbf{p}\in P} J_{\mathbf{p}}(\mathbf{w})^T \mathbf{e}_{\mathbf{p}}(\mathbf{w}), \tag{2.7}$$

with $\mu \geq 0$ and I the identity matrix of size $|\mathcal{V}| \times |\mathcal{V}|$. Note that if $\mu = 0$ we recover Newton's method (2.6), while for $\mu \gg 1$ the search direction $\Delta\mathbf{w}$ approaches the antigradient of E. Hence, the Levenberg-Marquardt algorithm can be seen as an interpolation between Newton's method and the steepest descent method, aiming to retain the advantages of both techniques [23].

The Levenberg-Marquardt training algorithm proceeds as follows. At each epoch t of the training procedure, we solve the (potentially large) linear system (2.7). Whenever the step $\Delta\mathbf{w}(t)$ leads to a reduction in the performance function, i.e., $E(\mathbf{w}(t) + \Delta\mathbf{w}(t)) < E(\mathbf{w}(t))$, the parameter μ is reduced by a factor $\beta > 1$. Conversely, if $E(\mathbf{w}(t) + \Delta\mathbf{w}(t)) > E(\mathbf{w}(t))$ the parameter is multiplied by the same factor β. This reflects the idea that far from the actual minimum we should prefer the gradient method to Newton's method, since the latter may diverge. Yet, once in a neighborhood of the minimum, we switch to Newton's method so to exploit its faster convergence [42].

The key step in the algorithm is the computation of the Jacobian $J_{\mathbf{p}}(\mathbf{w})$ for each training vector $\mathbf{p}$. Suppose that the k-th element w_k of $\mathbf{w}$ represents the weight $w_{i,j}$ of the connection (i,j), for some i and j, with $1 \leq i,j \leq |\mathcal{N}|$, i.e., $w_k = w_{i,j}$. Then:

$$\frac{\partial e_{\mathbf{p},h}}{\partial w_{i,j}} = \frac{\partial e_{\mathbf{p},h}}{\partial u_{\mathbf{p},j}} \frac{\partial u_{\mathbf{p},j}}{\partial w_{i,j}} = \frac{\partial e_{\mathbf{p},h}}{\partial y_{\mathbf{p},j}} \frac{\partial y_{\mathbf{p},j}}{\partial u_{\mathbf{p},j}} \frac{\partial u_{\mathbf{p},j}}{\partial w_{i,j}} = \frac{\partial e_{\mathbf{p},h}}{\partial y_{\mathbf{p},j}} f'_{act}(u_{\mathbf{p},j})\, y_{\mathbf{p},i} = \delta_{\mathbf{p},h,j}\, y_{\mathbf{p},i},$$

with

$$\delta_{\mathbf{p},h,j} := -\frac{\partial e_{\mathbf{p},h}}{\partial u_{\mathbf{p},j}} = -\frac{\partial e_{\mathbf{p},h}}{\partial y_{\mathbf{p},j}} f'_{act}(u_{\mathbf{p},j}). \tag{2.8}$$

For the computation of the derivative

$$\frac{\partial e_{\mathbf{p},h}}{\partial y_{\mathbf{p},j}}$$

occurring in (2.8), we assume that, within the set of neurons $\mathcal{N}$, items are ordered such that the output neurons come first, i.e.,

$$j \text{ output neuron} \quad \Leftrightarrow \quad 1 \leq j \leq M_O\,.$$

We can then distinguish three cases:

(i) j output neuron, $j = h$: since $e_{\mathbf{p},h} = e_{\mathbf{p},j} = t_{\mathbf{p},j} - y_{\mathbf{p},j}$, then

$$\frac{\partial e_{\mathbf{p},h}}{\partial y_{\mathbf{p},j}} = -1\,;$$

(ii) j output neuron, $j \neq h$: the output of an output neuron can not influence the signal fired by another output neuron, hence

$$\frac{\partial e_{\mathbf{p},h}}{\partial y_{\mathbf{p},j}} = 0\,;$$

(iii) j inner neuron: letting R be the set of successors of j, the chain rule yields

$$\frac{\partial e_{\mathbf{p},h}}{\partial y_{\mathbf{p},j}} = \sum_{r \in R} \frac{\partial e_{\mathbf{p},h}}{\partial u_{\mathbf{p},r}} \frac{\partial u_{\mathbf{p},r}}{\partial y_{\mathbf{p},j}} = -\sum_{r \in R} \delta_{\mathbf{p},h,r}\; w_{j,r}\,.$$

Ultimately, at any iteration of the learning algorithm, the entries of the Jacobian matrix $J_\mathbf{p}$ are given by

$$\frac{\partial e_{\mathbf{p},h}}{\partial w_k} = \delta_{\mathbf{p},h,j}\; y_{\mathbf{p},i}\,, \quad 1 \leq h \leq M_O\,, 1 \leq k \leq |\mathscr{V}|\,, w_k = w_{i,j} \text{ for some } i \text{ and } j\,,$$

with

$$\delta_{\mathbf{p},h,j} = \begin{cases} f'_{act}(u_{\mathbf{p},j}) \sum_{r \in R} \delta_{\mathbf{p},h,r}\; w_{j,r}\,, & \text{if } j \text{ inner neuron}\,, \quad (2.9a) \\ f'_{act}(u_{\mathbf{p},j})\; \delta^K_{jh}\,, & \text{if } j \text{ output neuron}\,, \quad (2.9b) \end{cases}$$

where δ^K_{jh} is the Kronecker delta. Observe that (2.9a) defines $\delta_{\mathbf{p},h,j}$ for a hidden node j by relying on the neurons in the following layer, whereas (2.9b) only involves the net input $u_{\mathbf{p},j}$ of the neuron itself. Therefore, the coupled equations (2.9a)-(2.9b) implicitly set the order in which the entries of $J_\mathbf{p}(\mathbf{w})$ have to be determined: starting from the output layer, compute the terms related to connections ending in that layer, then move backwards to the preceeding layer. In this way, the error is *backpropagated* from the output down to the input, leaving traces in each layer of the network [38, 61].

Let us finally remark that a trial and error approach is required to find satisfactory values for μ and β; as proposed in [42], a good starting point may be $\mu = 0.01$, with $\beta = 10$. Moreover, the dimension of the system (2.7) increases nonlinearly with the number of neurons in the network, making the Levenberg-Marquardt algorithm poorly efficient for large networks [23]. However, it turns out to be efficient and accurate for networks with few hundreads of connections.

3. Parametrized partial differential equations

Assume $\mathscr{P}_{ph} \subset \mathbb{R}^{P_{ph}}$ and $\mathscr{P}_g \subset \mathbb{R}^{P_g}$ be compact sets, and let $\boldsymbol{\mu}_{ph} \in \mathscr{P}_{ph}$ and $\boldsymbol{\mu}_g \in \mathscr{P}_g$ be respectively the *physical* and *geometrical* parameters characterizing the differential problem, so that $\boldsymbol{\mu} = (\boldsymbol{\mu}_{ph}, \boldsymbol{\mu}_g) \in \mathscr{P} = \mathscr{P}_{ph} \times \mathscr{P}_g \subset \mathbb{R}^P$, $P = P_{ph} + P_g$ represents the overall *input vector parameter*. While $\boldsymbol{\mu}_{ph}$ addresses material properties, source terms and boundary conditions, $\boldsymbol{\mu}_g$ defines the shape of the computational domain $\widetilde{\Omega} = \widetilde{\Omega}(\boldsymbol{\mu}_g) \subset \mathbb{R}^d$, $d = 1, 2$, with Lipschitz boundary $\widetilde{\Gamma} = \partial\widetilde{\Omega}$; we denote by $\widetilde{\Gamma}_D$ and $\widetilde{\Gamma}_N$ the portions of $\widetilde{\Gamma}$ where Dirichlet and Neumann boundary conditions are enforced, with $\widetilde{\Gamma}_D \cup \widetilde{\Gamma}_N = \widetilde{\Gamma}$ and $\mathring{\widetilde{\Gamma}}_D \cap \mathring{\widetilde{\Gamma}}_N = \emptyset$.

Consider then a Hilbert space $\widetilde{V} = \widetilde{V}(\boldsymbol{\mu}_g) = \widetilde{V}(\widetilde{\Omega}(\boldsymbol{\mu}_g))$ defined over the domain $\widetilde{\Omega}(\boldsymbol{\mu}_g)$, equipped with the scalar product $(\cdot,\cdot)_{\widetilde{V}}$ and the induced norm $\|\cdot\|_{\widetilde{V}} = \sqrt{(\cdot,\cdot)_{\widetilde{V}}}$. Furthermore, let $\widetilde{V}' = \widetilde{V}'(\boldsymbol{\mu}_g)$ be the dual of $\widetilde{V}$, i.e., the space of linear and continuous functionals over $\widetilde{V}$. Denoting by $\widetilde{G} : \widetilde{V} \times \mathscr{P}_{ph} \to \widetilde{V}'$ the map representing a parametrized nonlinear second-order

PDE, the differential (strong) form of the problem of interest reads: given $\boldsymbol{\mu} = (\boldsymbol{\mu}_{ph}, \boldsymbol{\mu}_g) \in \mathscr{P}$, find $\widetilde{u}(\boldsymbol{\mu}) \in \widetilde{V}(\boldsymbol{\mu}_g)$ such that

$$\widetilde{G}(\widetilde{u}(\boldsymbol{\mu}); \boldsymbol{\mu}_{ph}) = 0 \quad \text{in } \widetilde{V}'(\boldsymbol{\mu}_g)\,, \tag{3.1}$$

namely

$$\langle \widetilde{G}(\widetilde{u}(\boldsymbol{\mu}); \boldsymbol{\mu}_{ph}),\, v \rangle_{\widetilde{V}',\widetilde{V}} = 0 \quad \forall v \in \widetilde{V}(\boldsymbol{\mu}_g)\,.$$

Here, $\langle \cdot, \cdot \rangle_{\widetilde{V}',\widetilde{V}} : \widetilde{V}' \times \widetilde{V} \to \mathbb{R}$ represents the duality pairing between $\widetilde{V}'$ and $\widetilde{V}$, encoding the action of any functional of $\widetilde{V}'$ onto elements of $\widetilde{V}$.

The finite element method requires problem (3.1) to be stated in a weak (or variational) form [52]. To this end, let us introduce the form $\widetilde{g} : \widetilde{V} \times \widetilde{V} \times \mathscr{P} \to \mathbb{R}$, with $g(\cdot, \cdot; \boldsymbol{\mu})$ defined as:

$$\widetilde{g}(w, v; \boldsymbol{\mu}) = \langle \widetilde{G}(w; \boldsymbol{\mu}_{ph}); v \rangle_{\widetilde{V}',\widetilde{V}} \quad \forall w, v \in \widetilde{V}\,.$$

The variational formulation of (3.1) then reads: given $\boldsymbol{\mu} = (\boldsymbol{\mu}_{ph}, \boldsymbol{\mu}_g) \in \mathscr{P}$, find $\widetilde{u}(\boldsymbol{\mu}) \in \widetilde{V}(\boldsymbol{\mu}_g)$ such that

$$\widetilde{g}(\widetilde{u}(\boldsymbol{\mu}), v; \boldsymbol{\mu}) = 0 \quad \forall v \in \widetilde{V}(\boldsymbol{\mu})\,.$$

Note that the definition of $\widetilde{g}(\cdot, \cdot; \boldsymbol{\mu})$ relies on the duality pairing $\langle \cdot, \cdot \rangle_{\widetilde{V}',\widetilde{V}}$ between $\widetilde{V}$ and $\widetilde{V}'$. Hence, from the nonlinearity of $\widetilde{G}$ follows the nonlinearity of $\widetilde{g}$ with respect to its first argument.

3.1. From physical to reference domain

As anticipated in the Introduction, any reduced basis method seeks an approximated solution to a differential problem as a combination of (few) well-chosen basis vectors. These typically result from a suitable combination of a collection of high-fidelity approximations, called *snapshots*. Therefore, when addressing problems defined on variable shape domains, ensuring the *compatibility* among snapshots is crucial. To this end, we formulate and solve the differential problem over a fixed, *parameter-independent* domain Ω. This can be accomplished upon introducing a parametrized map $\boldsymbol{\Phi} : \Omega \times \mathscr{P}_g \to \widetilde{\Omega}$ such that

$$\widetilde{\Omega}(\boldsymbol{\mu}_g) = \boldsymbol{\Phi}(\Omega; \boldsymbol{\mu}_g)\,.$$

The transformation $\boldsymbol{\Phi}$ allows to restate the general problem (3.1). Let V be a suitable Hilbert space over Ω and V' be its dual. Suppose V is equipped with the scalar product $(\cdot, \cdot)_V : V \times V \to \mathbb{R}$ and the induced norm $\|\cdot\|_V = \sqrt{(\cdot, \cdot)_V} : V \to [0, \infty)$. Given the parametrized map $G : V \times \mathscr{P} \to V'$ representing the (nonlinear) PDE over the reference domain Ω, we focus on differential problems of the form: given $\boldsymbol{\mu} \in \mathscr{P}$, find $u(\boldsymbol{\mu}) \in V$ such that

$$G(u(\boldsymbol{\mu}); \boldsymbol{\mu}) = 0 \quad \text{in } V'\,. \tag{3.2}$$

The weak formulation of problem (3.2) reads: given $\boldsymbol{\mu} \in \mathscr{P}$, seek $u(\boldsymbol{\mu}) \in V$ such that

$$g(u(\boldsymbol{\mu}), v; \boldsymbol{\mu}) = 0 \quad \forall v \in V\,, \tag{3.3}$$

where $g : V \times V \times \mathscr{P} \to \mathbb{R}$ is defined as

$$g(w, v; \boldsymbol{\mu}) = \langle G(w); \boldsymbol{\mu}),\, v \rangle_{V',V} \quad \forall w, v \in V\,,$$

with $\langle \cdot, \cdot \rangle_{V',V} : V' \times V \to \mathbb{R}$ the dual pairing between V and V'. Observe that the explicit expression of $g(\cdot, \cdot; \boldsymbol{\mu})$ involves the map $\boldsymbol{\Phi}$, thus keeping track of the original domain $\widetilde{\Omega}(\boldsymbol{\mu}_g)$. Then, the solution $\widetilde{u}(\boldsymbol{\mu})$ over the original domain $\widetilde{\Omega}(\boldsymbol{\mu}_g)$ can be recovered as

$$\widetilde{u}(\boldsymbol{\mu}) = u(\boldsymbol{\mu}) \circ \boldsymbol{\Phi}(\boldsymbol{\mu})\,.$$

For any $\boldsymbol{\mu} \in \mathscr{P}$ we seek a discrete solution $u_h(\boldsymbol{\mu})$ to the problem (3.2) on a *parameter-independent* cover Ω_h of the domain Ω. Provided a convenient choice for Ω, this makes the mesh generation process easier. In addition, we note that discretizing the problem (3.2) over Ω_h is equivalent to approximating the original problem (3.1) over the mesh $\widetilde{\Omega}_h(\boldsymbol{\mu}_g)$, given by

$$\widetilde{\Omega}_h(\boldsymbol{\mu}_g) = \boldsymbol{\Phi}(\Omega_h; \boldsymbol{\mu}_g)\,.$$

In our numerical tests, we employ the squared reference domain shown on the right in Fig. 7.3 and we resort to a particular choice for $\mathbf{\Phi}$ - the boundary displacement-dependent transfinite map (BDD TM) proposed in [34].

3.2. *Problems of interest*

Within the wide range of PDEs which suit the functional framework portrayed so far, in this work we focus on two relevant examples - the nonlinear Poisson equation and the stationary Navier-Stokes equations - which will serve as test cases in Section 7.

3.2.1. *Nonlinear Poisson equation*

Despite a rather simple form, the Poisson equation has proved itself to be effective to model steady phenomena occurring in, e.g., electromagnetism, heat transfer, and underground flows [44]. We consider the following version of the parametrized Poisson equation for a state variable $\widetilde{u} = \widetilde{u}(\boldsymbol{\mu})$:

$$\begin{cases} -\widetilde{\nabla} \cdot \left(\widetilde{k}(\widetilde{\boldsymbol{x}}, \widetilde{u}(\boldsymbol{\mu}); \boldsymbol{\mu}_{ph}) \, \widetilde{\nabla} \widetilde{u}(\boldsymbol{\mu}) \right) = \widetilde{s}(\widetilde{\boldsymbol{x}}; \boldsymbol{\mu}_{ph}) & \text{in } \widetilde{\Omega}(\boldsymbol{\mu}_g), \quad (3.4a) \\ \widetilde{u}(\boldsymbol{\mu}) = \widetilde{g}(\widetilde{\boldsymbol{\sigma}}; \boldsymbol{\mu}_{ph}) & \text{on } \widetilde{\Gamma}_D, \quad (3.4b) \\ \widetilde{k}(\widetilde{\boldsymbol{\sigma}}, \widetilde{u}(\boldsymbol{\mu}); \boldsymbol{\mu}_{ph}) \, \widetilde{\nabla} \widetilde{u}(\boldsymbol{\mu}) \cdot \widetilde{\boldsymbol{n}} = 0 & \text{on } \widetilde{\Gamma}_N. \quad (3.4c) \end{cases}$$

Here, for any $\boldsymbol{\mu}_g \in \mathscr{P}_g$, $\widetilde{\boldsymbol{x}}$ and $\widetilde{\boldsymbol{\sigma}}$ denote a generic point in $\widetilde{\Omega}$ and on $\widetilde{\Gamma}$, respectively, $\widetilde{\nabla}$ is the nabla operator with respect to $\widetilde{\boldsymbol{x}}$, $\widetilde{\boldsymbol{n}} = \widetilde{\boldsymbol{n}}(\widetilde{\boldsymbol{\sigma}})$ denotes the outward normal to $\widetilde{\Gamma}$ in $\widetilde{\boldsymbol{\sigma}}$, $\widetilde{k} : \widetilde{\Omega} \times \mathbb{R} \times \mathscr{P}_{ph} \to (0,\infty)$ is the diffusion coefficient, $\widetilde{s} : \widetilde{\Omega} \times \mathscr{P}_{ph} \to \mathbb{R}$ is the source term, and $\widetilde{g} : \widetilde{\Gamma}_D \times \mathscr{P}_{ph} \to \mathbb{R}$ encodes the Dirichlet boundary conditions. We should point out that, to ease the subsequent discussion, we limit the attention to homogeneous Neumann boundary constraints.

Let us fix $\boldsymbol{\mu} \in \mathscr{P}$ and set

$$\widetilde{V} = H^1_{\widetilde{\Gamma}_D}(\widetilde{\Omega}) = \left\{ v \in H^1(\widetilde{\Omega}) \, : \, v\big|_{\widetilde{\Gamma}_D} = 0 \right\},$$

Multiplying (3.4a) by a *test* function $v \in \widetilde{V}$, integrating over $\widetilde{\Omega}$, and exploiting integration by parts on the left-hand side, yields:

$$\int_{\widetilde{\Omega}(\boldsymbol{\mu}_g)} \widetilde{k}(\widetilde{u}(\boldsymbol{\mu}); \boldsymbol{\mu}_{ph}) \, \widetilde{\nabla} \widetilde{u}(\boldsymbol{\mu}) \cdot \widetilde{\nabla} v \, d\widetilde{\Omega}(\boldsymbol{\mu}_g) = \int_{\widetilde{\Omega}(\boldsymbol{\mu}_g)} \widetilde{s}(\boldsymbol{\mu}_{ph}) \, v \, d\widetilde{\Omega}(\boldsymbol{\mu}_g), \tag{3.5}$$

where we have omitted the dependence on the space variable $\widetilde{\boldsymbol{x}}$ for ease of notation. For the integrals in Eq. (3.5) to be well-defined, we require, for any $\boldsymbol{\mu}_g \in \mathscr{P}_g$,

$$|\widetilde{k}(\widetilde{\boldsymbol{x}}, r; \boldsymbol{\mu}_g)| < \infty \text{ for almost any (a.a.) } \widetilde{\boldsymbol{x}} \in \widetilde{\Omega}(\boldsymbol{\mu}_g), \, r \in \mathbb{R} \quad \text{and} \quad \widetilde{s}(\boldsymbol{\mu}_{ph}) \in L^2\big(\widetilde{\Omega}(\boldsymbol{\mu}_g)\big).$$

Let then $\widetilde{l} = \widetilde{l}(\boldsymbol{\mu}) \in H^1\big(\widetilde{\Omega}(\boldsymbol{\mu}_g)\big)$ be a *lifting* function such that $\widetilde{l}(\boldsymbol{\mu})\big|_{\widetilde{\Gamma}_D} = \widetilde{g}(\boldsymbol{\mu}_{ph})$, with $\widetilde{g}(\boldsymbol{\mu}_{ph}) \in H^{1/2}\big(\widetilde{\Gamma}_D\big)$. We assume that such a function can be constructed, e.g., by interpolation of the boundary condition. Hence, upon defining

$$\begin{aligned} \widetilde{a}(w, v; \boldsymbol{\mu}) &:= \int_{\widetilde{\Omega}(\boldsymbol{\mu}_g)} \widetilde{k}(w + \widetilde{l}(\boldsymbol{\mu}); \boldsymbol{\mu}_{ph}) \, \widetilde{\nabla} w \cdot \widetilde{\nabla} v \, d\widetilde{\Omega}(\boldsymbol{\mu}_g) + \int_{\widetilde{\Omega}(\boldsymbol{\mu}_g)} \widetilde{k}(w + \widetilde{l}(\boldsymbol{\mu}); \boldsymbol{\mu}_{ph}) \, \widetilde{\nabla} \widetilde{l}(\boldsymbol{\mu}) \cdot \widetilde{\nabla} v \, d\widetilde{\Omega}(\boldsymbol{\mu}_g) \quad && \forall w, v \in \widetilde{V}(\boldsymbol{\mu}_g), \\ \widetilde{f}(v; \boldsymbol{\mu}) &:= \int_{\widetilde{\Omega}(\boldsymbol{\mu}_g)} \widetilde{s}(\boldsymbol{\mu}_{ph}) \, v \, d\widetilde{\Omega}(\boldsymbol{\mu}_g) && \forall v \in \widetilde{V}(\boldsymbol{\mu}_g), \end{aligned}$$

the weak formulation of problem (3.4) reads: given $\boldsymbol{\mu} \in \mathscr{P}$, find $\widetilde{u}(\boldsymbol{\mu}) \in \widetilde{V}(\boldsymbol{\mu}_g)$ such that

$$\widetilde{a}(\widetilde{u}(\boldsymbol{\mu}), v; \boldsymbol{\mu}) = \widetilde{f}(v; \boldsymbol{\mu}) \quad \forall v \in \widetilde{V}(\boldsymbol{\mu}_g), \tag{3.6}$$

Then, the weak solution of problem (3.4) is given by $\widetilde{u}(\boldsymbol{\mu}) + \widetilde{l}(\boldsymbol{\mu})$. Note that using a lifting function makes the formulation (3.6) *symmetric*, i.e., both the solution and the test functions are picked up from the same functional space [52].

Let us now re-state the variational problem (3.6) onto the reference domain Ω. For this purpose, let Γ_D and Γ_N be the portions of the boundary $\Gamma = \partial\Omega$ on which we impose Dirichlet and Neumann boundary conditions, respectively. Moreover, we denote by $\mathbb{J}_{\boldsymbol{\Phi}}(\boldsymbol{\mu})$ the Jacobian of the parametrized map $\boldsymbol{\Phi}(\cdot;\boldsymbol{\mu})$, with determinant $|\mathbb{J}_{\boldsymbol{\Phi}}(\boldsymbol{\mu})|$, and we set

$$k(\boldsymbol{x},\cdot;\boldsymbol{\mu}) = \widetilde{k}(\boldsymbol{\Phi}(\boldsymbol{x};\boldsymbol{\mu}),\cdot;\boldsymbol{\mu}), \quad s(\boldsymbol{x};\boldsymbol{\mu}) = \widetilde{s}(\boldsymbol{\Phi}(\boldsymbol{x};\boldsymbol{\mu});\boldsymbol{\mu}) \quad \text{and} \quad g(\boldsymbol{x};\boldsymbol{\mu}) = \widetilde{g}(\boldsymbol{\Phi}(\boldsymbol{x};\boldsymbol{\mu});\boldsymbol{\mu}).$$

Letting

$$V = H^1_{\Gamma_D}(\Omega)$$

and exploiting standard change of variables formulas, the variational formulation of the Poisson problem (3.4) over Ω reads: given $\boldsymbol{\mu} \in \mathscr{P}$, find $u(\boldsymbol{\mu}) \in V$ such that

$$a(u(\boldsymbol{\mu}), v; \boldsymbol{\mu}) = f(v;\boldsymbol{\mu}) \quad \forall v \in V,$$

with

$$\begin{aligned} a(w,v;\boldsymbol{\mu}) = &\int_\Omega k(w + l(\boldsymbol{\mu});\boldsymbol{\mu})\, \mathbb{J}_{\boldsymbol{\Phi}}^{-T}(\boldsymbol{\mu})\nabla w \cdot \mathbb{J}_{\boldsymbol{\Phi}}^{-T}(\boldsymbol{\mu})\nabla v\, |\mathbb{J}_{\boldsymbol{\Phi}}(\boldsymbol{\mu})|\, d\Omega \\ &+ \int_\Omega k(w + l(\boldsymbol{\mu});\boldsymbol{\mu})\, \mathbb{J}_{\boldsymbol{\Phi}}^{-T}(\boldsymbol{\mu})\nabla l(\boldsymbol{\mu}) \cdot \mathbb{J}_{\boldsymbol{\Phi}}^{-T}(\boldsymbol{\mu})\nabla v\, |\mathbb{J}_{\boldsymbol{\Phi}}(\boldsymbol{\mu})|\, d\Omega, \end{aligned} \tag{3.7a}$$

$$f(v;\boldsymbol{\mu}) = \int_\Omega s(\boldsymbol{\mu})\; v\, |\mathbb{J}_{\boldsymbol{\Phi}}(\boldsymbol{\mu})|\, d\Omega, \tag{3.7b}$$

for any $w, v \in V$ and $\boldsymbol{\mu} \in \mathscr{P}$. Note that, as done in (3.2.1), we resort to a lifting function $l(\boldsymbol{\mu}) \in H^1(\Omega)$ with $l(\boldsymbol{\mu})\big|_{\Gamma_D} = g(\boldsymbol{\mu})$, such that the weak solution to problem (3.4) re-stated over Ω is obtained as $u(\boldsymbol{\mu}) + l(\boldsymbol{\mu})$.

Let us also remark that, when on a parameter-independent configuration, one can avoid to distinguish between physical and geometrical parameters, since even the latter now affect the integrands in (3.7a) and (3.7b), and not the domain of integration.

3.2.2. Steady uncompressible Navier-Stokes equations

The system of the Navier-Stokes equations model the conservation of mass and momentum for an incompressible Newtonian viscous fluid confined in a region $\widetilde{\Omega}(\boldsymbol{\mu}_g) \subset \mathbb{R}^d$, $d = 2, 3$ [54]. Letting $\widetilde{\boldsymbol{v}} = \widetilde{\boldsymbol{v}}(\widetilde{\boldsymbol{x}};\boldsymbol{\mu})$ and $\widetilde{p} = \widetilde{p}(\widetilde{\boldsymbol{x}};\boldsymbol{\mu})$ be the velocity and pressure of the fluid, respectively, the parametrized steady version of the Navier-Stokes equations considered in this work reads:

$$\begin{cases} \widetilde{\nabla}\cdot\widetilde{\boldsymbol{v}}(\boldsymbol{\mu}) = 0 & \text{in } \widetilde{\Omega}(\boldsymbol{\mu}_g), & (3.8a) \\ -\nu(\boldsymbol{\mu})\,\widetilde{\Delta}\widetilde{\boldsymbol{v}}(\boldsymbol{\mu}) + (\widetilde{\boldsymbol{v}}(\boldsymbol{\mu})\cdot\widetilde{\nabla})\widetilde{\boldsymbol{v}}(\boldsymbol{\mu}) + \dfrac{1}{\rho(\boldsymbol{\mu})}\widetilde{\nabla}\widetilde{p}(\boldsymbol{\mu}) = \boldsymbol{0} & \text{in } \widetilde{\Omega}(\boldsymbol{\mu}_g), & (3.8b) \\ \widetilde{\boldsymbol{v}}(\boldsymbol{\mu}) = \widetilde{\boldsymbol{g}}(\boldsymbol{\mu}_{ph}) & \text{on } \widetilde{\Gamma}_D(\boldsymbol{\mu}_g), & (3.8c) \\ \widetilde{p}(\boldsymbol{\mu})\widetilde{\boldsymbol{n}} - \nu(\boldsymbol{\mu})\widetilde{\nabla}\widetilde{\boldsymbol{v}}(\boldsymbol{\mu})\cdot\widetilde{\boldsymbol{n}} = \boldsymbol{0} & \text{on } \widetilde{\Gamma}_N(\boldsymbol{\mu}_g). & (3.8d) \end{cases}$$

Here, $\widetilde{\boldsymbol{g}}(\boldsymbol{\mu}_{ph})$ denotes the velocity field prescribed on $\widetilde{\Gamma}_D$, whereas homogeneous Neumann conditions are applied on $\widetilde{\Gamma}_N$. Furthermore, $\rho(\boldsymbol{\mu})$ and $\nu(\boldsymbol{\mu})$ represent the uniform density and kinematic viscosity of the fluid, respectively. Note that, despite these quantities encode physical properties, we let them depend on the geometrical parameters as well. Indeed, fluid dynamics can be characterized (and controlled) by means of a wealth of dimensionless quantities, e.g., the Reynolds number, which combine physical properties of the fluid with geometrical features of the domain. Therefore, a numerical study of the sensitivity of the system (3.8) with respect to $\boldsymbol{\mu}_g$ may be carried out by adapting either $\rho(\boldsymbol{\mu})$ or $\nu(\boldsymbol{\mu})$ as $\boldsymbol{\mu}_g$ varies, so to preserve a dimensionless quantity of interest; we refer the reader to Subsection 7.3 for a practical example.
For our purpose, it is worth noticing that the nonlinearity of problem (3.8) lies in the convective term

$$\big(\widetilde{\boldsymbol{v}}(\boldsymbol{\mu})\cdot\widetilde{\nabla}\big)\widetilde{\boldsymbol{v}}(\boldsymbol{\mu}),$$

which gives rise to a *quadratic* nonlinearity.

To write the differential system (3.8) in weak form over a $\boldsymbol{\mu}_g$-independent configuration Ω, let us introduce the velocity and pressure spaces

$$\widetilde{X}(\boldsymbol{\mu}_g) = \big[H^1_{\widetilde{\Gamma}_D}\big(\widetilde{\Omega}(\boldsymbol{\mu}_g)\big)\big]^d \quad \text{and} \quad \widetilde{Q}(\boldsymbol{\mu}_g) = L^2\big(\widetilde{\Omega}(\boldsymbol{\mu}_g)\big),$$

respectively, with

$$X = \left[H^1_{\Gamma_D}(\Omega)\right]^d \text{ and } Q = L^2(\Omega)$$

be their respective counterparts over Ω. By multiplying (3.8) for test functions $\left(\widetilde{\boldsymbol{\chi}}, \widetilde{\xi}\right) \in \widetilde{X}(\boldsymbol{\mu}_g) \times \widetilde{Q}(\boldsymbol{\mu}_g)$, integrating by parts and then tracing everything back onto Ω by means of the parametrized map $\boldsymbol{\Phi}(\cdot; \boldsymbol{\mu})$, we end up with the following parametrized weak variational problem: given $\boldsymbol{\mu} \in \mathscr{P}$, find $u(\boldsymbol{\mu}) = (\boldsymbol{v}(\boldsymbol{\mu}), p(\boldsymbol{\mu})) \in V = X \times Q$ so that

$$\begin{aligned} a(\boldsymbol{v}(\boldsymbol{\mu}), \boldsymbol{\chi}; \boldsymbol{\mu}) + c(\boldsymbol{v}(\boldsymbol{\mu}), \boldsymbol{v}(\boldsymbol{\mu}), \boldsymbol{\chi}; \boldsymbol{\mu}) + d(\boldsymbol{v}(\boldsymbol{\mu}), \boldsymbol{\chi}; \boldsymbol{\mu}) + b(p(\boldsymbol{\mu}), \nabla \cdot \boldsymbol{\chi}; \boldsymbol{\mu}) &= f_1(\boldsymbol{\chi}; \boldsymbol{\mu}), \\ b(\nabla \cdot \boldsymbol{v}(\boldsymbol{\mu}), \xi; \boldsymbol{\mu}) &= f_2(\xi; \boldsymbol{\mu}), \end{aligned}$$

for all $(\boldsymbol{\chi}, \xi) \in V$, with, for any $\boldsymbol{\mu} \in \mathscr{P}$

$$\begin{aligned} c(\boldsymbol{\psi}, \boldsymbol{\chi}, \boldsymbol{\eta}; \boldsymbol{\mu}) &= \int_\Omega \left(\boldsymbol{\psi} \cdot \mathbb{J}_{\boldsymbol{\Phi}}^{-T}(\boldsymbol{\mu}) \nabla\right) \boldsymbol{\chi} \cdot \boldsymbol{\eta} \, |\mathbb{J}_{\boldsymbol{\Phi}}(\boldsymbol{\mu})| \, d\Omega, & d(\boldsymbol{\psi}, \boldsymbol{\chi}; \boldsymbol{\mu}) &= c(\boldsymbol{l}(\boldsymbol{\mu}), \boldsymbol{\psi}, \boldsymbol{\chi}; \boldsymbol{\mu}) + c(\boldsymbol{\psi}, \boldsymbol{l}(\boldsymbol{\mu}), \boldsymbol{\chi}; \boldsymbol{\mu}), \\ a(\boldsymbol{\psi}, \boldsymbol{\chi}; \boldsymbol{\mu}) &= \nu(\boldsymbol{\mu}) \int_\Omega \mathbb{J}_{\boldsymbol{\Phi}}^{-T}(\boldsymbol{\mu}) \nabla \boldsymbol{\psi} : \mathbb{J}_{\boldsymbol{\Phi}}^{-T}(\boldsymbol{\mu}) \nabla \boldsymbol{\chi} \, |\mathbb{J}_{\boldsymbol{\Phi}}(\boldsymbol{\mu})| \, d\Omega, & f_1(\boldsymbol{\psi}; \boldsymbol{\mu}) &= -a(\boldsymbol{l}(\boldsymbol{\mu}), \boldsymbol{\psi}; \boldsymbol{\mu}) - c(\boldsymbol{l}(\boldsymbol{\mu}), \boldsymbol{l}(\boldsymbol{\mu}), \boldsymbol{\psi}; \boldsymbol{\mu}), \\ b(\boldsymbol{\psi}, \xi; \boldsymbol{\mu}) &= -\frac{1}{\rho(\boldsymbol{\mu})} \int_\Omega \left(\mathbb{J}_{\boldsymbol{\Phi}}^{-T}(\boldsymbol{\mu}) \nabla \cdot \boldsymbol{\psi}\right) \xi \, |\mathbb{J}_{\boldsymbol{\Phi}}(\boldsymbol{\mu})| \, d\Omega, & f_2(\xi; \boldsymbol{\mu}) &= -b(\boldsymbol{l}(\boldsymbol{\mu}), \xi; \boldsymbol{\mu}), \end{aligned}$$

for all $\boldsymbol{\psi}, \boldsymbol{\chi}, \boldsymbol{\eta} \in X$ and $\xi \in Q$. In the definitions of $d(\cdot, \cdot; \boldsymbol{\mu})$, $f_1(\cdot; \boldsymbol{\mu})$ and $f_2(\cdot; \boldsymbol{\mu})$, $\boldsymbol{l}(\boldsymbol{\mu}) \in \left[H^1(\Omega)\right]^d$ denotes the lifting vector field, with $\boldsymbol{l}(\boldsymbol{\mu})\big|_{\Gamma_D} = \boldsymbol{g}(\boldsymbol{\mu})$, $\boldsymbol{g}(\boldsymbol{x}; \boldsymbol{\mu}) = \widetilde{\boldsymbol{g}}(\boldsymbol{\Phi}(\boldsymbol{x}; \boldsymbol{\mu}); \boldsymbol{\mu})$ being the velocity field prescribed on Γ_D. Hence, the weak solution to (3.8) defined over the fixed domain Ω is given by $\left(\boldsymbol{v}(\boldsymbol{\mu}) + \boldsymbol{l}(\boldsymbol{\mu}), p(\boldsymbol{\mu})\right)$.

4. Discrete full-order model

Let $V_h \subset V$ be a finite-dimensional subspace of V of dimension M. The FE approximation of the weak problem (3.3) can be cast in the form: given $\boldsymbol{\mu} \in \mathscr{P}$, find $u_h(\boldsymbol{\mu}) \in V_h$ such that

$$g(u_h(\boldsymbol{\mu}), v_h; \boldsymbol{\mu}) = 0 \quad \forall v_h \in V_h. \tag{4.1}$$

The discretization (4.1) is known as *Galerkin approximation*, and therefore $u_h(\boldsymbol{\mu})$ is referred to as the *Galerkin solution* to the problem (3.2).

Due to the nonlinearity of $g(\cdot, \cdot; \boldsymbol{\mu})$ in its first argument, one has to resort to some iterative method, e.g., Newton's method, to solve the Galerkin problem (4.1). In this regard, let

$$dg[z](\cdot, \cdot; \boldsymbol{\mu}) : V \times V \to \mathbb{R}$$

be the partial Frechét derivative of $g(\cdot, \cdot; \boldsymbol{\mu})$ with respect to its first argument, evaluated at $z \in V$. Starting from an initial guess $u_h^0(\boldsymbol{\mu})$, we construct a collection of approximations $\left\{u_h^k(\boldsymbol{\mu})\right\}_{k \geq 0}$ to the Galerkin solution $u_h(\boldsymbol{\mu})$ by iteratively solving the linearized problems

$$dg\left[u_h^k(\boldsymbol{\mu})\right](\delta u_h^k(\boldsymbol{\mu}), v_h; \boldsymbol{\mu}) = -g(u_h^k(\boldsymbol{\mu}), v_h; \boldsymbol{\mu}) \quad \forall v_h \in V_h$$

in the unknown $\delta u_h^k(\boldsymbol{\mu}) \in V_h$, and then setting $u_h^{k+1}(\boldsymbol{\mu}) = u_h^k(\boldsymbol{\mu}) + \delta u_h^k(\boldsymbol{\mu})$.

To derive the algebraic counterpart of the Galerkin-Newton method, let $\left\{\phi_1, \dots, \phi_M\right\}$ be a basis for the M-dimensional space V_h, so that the solution $u_h(\boldsymbol{\mu})$ can be expressed as a linear combination of the basis functions, i.e.,

$$u_h(\boldsymbol{x}; \boldsymbol{\mu}) = \sum_{j=1}^{M} u_h^{(j)}(\boldsymbol{\mu}) \, \phi_j(\boldsymbol{x}).$$

Hence, denoting by $\mathbf{u}_h(\boldsymbol{\mu}) \in \mathbb{R}^M$ the vector collecting the *degrees of freedom* $\left\{u_h^{(j)}\right\}_{j=1}^M$ and exploiting the linearity of $g(\cdot, \cdot; \boldsymbol{\mu})$

in the second argument, the problem (4.1) is equivalent to: given $\boldsymbol{\mu} \in \mathscr{P}$, find $\mathbf{u}_h(\boldsymbol{\mu}) \in \mathbb{R}^M$ such that

$$g\left(\sum_{j=1}^{M} u_h^{(j)}(\boldsymbol{\mu})\,\phi_j, \phi_i; \boldsymbol{\mu}\right) = 0 \quad \forall i = 1, \dots, M.$$

We observe now that the above problem can be written in compact form as

$$\mathbf{G}_h(\mathbf{u}_h(\boldsymbol{\mu}); \boldsymbol{\mu}) = \mathbf{0} \in \mathbb{R}^M, \tag{4.2}$$

where the i-th component of the *residual vector* $\mathbf{G}(\cdot; \boldsymbol{\mu}) \in \mathbb{R}^M$ is given by

$$\left(\mathbf{G}_h(\mathbf{u}_h(\boldsymbol{\mu}); \boldsymbol{\mu})\right)_i = g\left(\sum_{j=1}^{M} u_h^{(j)}(\boldsymbol{\mu})\,\phi_j, \phi_i; \boldsymbol{\mu}\right), \quad i = 1, \dots, M. \tag{4.3}$$

Then, for $k \geq 0$, the k-th iteration of Newton's method applied to the system (4.2) entails the resolution of the *linear* system

$$\mathbb{J}_h\left(\mathbf{u}_h^k(\boldsymbol{\mu}); \boldsymbol{\mu}\right) \delta\mathbf{u}_h^k(\boldsymbol{\mu}) = -\mathbf{G}_h\left(\mathbf{u}_h^k(\boldsymbol{\mu}); \boldsymbol{\mu}\right), \quad \delta\mathbf{u}_h^k(\boldsymbol{\mu}) \in \mathbb{R}^M, \tag{4.4}$$

so that $\mathbf{u}_h^{k+1}(\boldsymbol{\mu}) = \mathbf{u}_h^k(\boldsymbol{\mu}) + \delta\mathbf{u}_h^k(\boldsymbol{\mu})$. Here, $\mathbb{J}_h(\cdot; \boldsymbol{\mu}) \in \mathbb{R}^{M \times M}$ denotes the Jacobian of the residual vector $\mathbf{G}_h(\cdot; \boldsymbol{\mu})$; exploiting the bilinearity of $dg[z](\cdot, \cdot; \boldsymbol{\mu})$, $\mathbb{J}_h(\cdot; \boldsymbol{\mu})$ is defined as

$$\left(\mathbb{J}_h\left(\mathbf{u}_h^k(\boldsymbol{\mu}); \boldsymbol{\mu}\right)\right)_{i,j} = dg\left[u_h^k(\boldsymbol{\mu})\right](\phi_j, \phi_i; \boldsymbol{\mu}), \quad i, j = 1, \dots, M.$$

5. Projection-based reduced basis method

As detailed in the previous section, the finite element discretization of the $\boldsymbol{\mu}$-dependent nonlinear differential problem (3.3), combined with Newton's method, entails the assembly and resolution of (possibly) many linear systems of the form (4.4), whose dimension is directly related to (i) the size of the underlying grid and (ii) the order of the polynomial FE spaces adopted. Since the accuracy of the resulting discretization heavily relies on these two factors, a direct numerical approximation of the full-order model implies severe computational costs. Therefore, this approach is hardly affordable in *many-query* and *real-time* contexts, even resorting to high-performance parallel workstations. This motivates the broad use of *reduced-order* models, across several inter-disciplinary areas, e.g., parameter estimation, optimal control, shape optimization and uncertainty quantification [30, 53].

Reduced basis methods seek an approximated solution to the problem (3.3) as a linear combination of parameter-independent functions

$$\{\psi_1, \dots, \psi_L\} \subset V_h,$$

called *reduced basis functions*, built from a collection of high-fidelity solutions

$$\{u_h(\boldsymbol{\mu}^{(1)}), \dots, u_h(\boldsymbol{\mu}^{(N)})\} \subset \mathscr{M}_h,$$

called *snapshots*, where the discrete and finite set

$$\Xi_N = \{\boldsymbol{\mu}^{(1)}, \dots, \boldsymbol{\mu}^{(N)}\} \subset \mathscr{P}$$

may consist of either a uniform lattice or randomly generated points over the parameter domain $\mathscr{P}$ [30]. The basis functions $\{\psi_l\}_{l=1}^L$ generally follow from a principal component analysis (PCA) of the set of snapshots (in that case, $N > L$), or they might coincide with the snapshots themselves (in that case, $N = L$). In the latter approach, typical of any *greedy* method, the parameters $\{\boldsymbol{\mu}^{(n)}\}_{n=1}^N$ must be carefully chosen according to some optimality criterium (see, e.g., [12]). Here, we pursue the first approach, employing the well-known Proper Orthogonal Decomposition (POD) method [60], detailed in the following subsection.

Assume now that a reduced basis is available and let $V_{\mathtt{rb}} \subset V_h$ be the associated *reduced basis space*, i.e.,

$$V_{\mathtt{rb}} = \mathrm{span}\{\psi_1, \dots, \psi_L\}.$$

A *reduced basis solution* $u_L(\boldsymbol{\mu})$ is sought in the form

$$u_L(\boldsymbol{x};\boldsymbol{\mu}) = \sum_{l=1}^{L} u_{\mathtt{rb}}^{(l)}(\boldsymbol{\mu})\, \psi_l(\boldsymbol{x}) \;\in\; V_{\mathtt{rb}},$$

with

$$\mathbf{u}_{\mathtt{rb}}(\boldsymbol{\mu}) = \left[u_{\mathtt{rb}}^{(1)}(\boldsymbol{\mu}), \dots, u_{\mathtt{rb}}^{(L)}(\boldsymbol{\mu})\right]^T \in \mathbb{R}^L$$

be the *coefficients* (also called *generalized coordinates*) for the expansion of the RB solution in the RB basis functions.

To unearth $u_L(\boldsymbol{\mu})$, we proceed to project the variational problem (3.3) onto the RB space $V_{\mathtt{rb}}$ by pursuing a standard Galerkin approach, leading to the following *reduced basis problem*: given $\boldsymbol{\mu} \in \mathscr{P}$, find $u_L(\boldsymbol{\mu}) \in V_{\mathtt{rb}}$ so that

$$g(u_L(\boldsymbol{\mu}), v_L; \boldsymbol{\mu}) = 0 \quad \forall v_L \in V_{\mathtt{rb}}. \tag{5.1}$$

Then, Newton's method applied to (5.1) entails, at each iteration $k \geq 0$, the solution of the linearized problem: given $\boldsymbol{\mu} \in \mathscr{P}$, seek $\delta u_L^k(\boldsymbol{\mu})$ such that

$$dg\left[u_L^k(\boldsymbol{\mu})\right]\left(\delta u_L^k(\boldsymbol{\mu}), v_L; \boldsymbol{\mu}\right) = -g\left(u_L^k(\boldsymbol{\mu}), v_L; \boldsymbol{\mu}\right) \quad \forall v_L \in V_{\mathtt{rb}},$$

with $u_L^{k+1}(\boldsymbol{\mu}) = u_L^k(\boldsymbol{\mu}) + \delta u_L^k(\boldsymbol{\mu})$.

Let us point out that the RB functions $\{\psi_l\}_{l=1}^L$ belong to V_h, i.e., they are actual FE functions. Hence, denoting by $\boldsymbol{\psi}_l \in \mathbb{R}^M$ the vector collecting the nodal values of ψ_l, for $l = 1, \dots, L$, we introduce the matrix

$$\mathbb{V} = \left[\boldsymbol{\psi}_1 \,|\, \dots \,|\, \boldsymbol{\psi}_L\right] \in \mathbb{R}^{M \times L}.$$

For any $v_L \in V_{\mathtt{rb}}$, the matrix $\mathbb{V}$ encodes the change of variables from the RB basis to the standard (Lagrangian) FE basis, i.e.,

$$\mathbf{v}_L = \mathbb{V}\, \mathbf{v}_{\mathtt{rb}}. \tag{5.2}$$

Therefore, each element v_L of the reduced space admits two (algebraic) representations:

- $\mathbf{v}_{\mathtt{rb}} \in \mathbb{R}^L$, collecting the coefficients for the expansion of v_L in terms of the RB basis $\{\psi_1, \dots, \psi_L\}$;
- $\mathbf{v}_L \in \mathbb{R}^M$, collecting the coefficients for the expansion of v_L in terms of the FE basis $\{\phi_1, \dots, \phi_M\}$.

Note that the latter is also available for any $v_h \in V_h$, while the former characterizes the element in the subspace $V_{\mathtt{rb}}$.

Upon choosing $v_L = \psi_l$, $l = 1, \dots, L$, in the RB problem (5.1), for any $\boldsymbol{\mu} \in \mathscr{P}$ we get the set of equations

$$g(u_L(\boldsymbol{\mu}), \psi_l; \boldsymbol{\mu}) = 0 \quad 1 \leq l \leq L. \tag{5.3}$$

Inserting into (5.3) the expansion of ψ_l, $l = 1, \dots, L$, in terms of the canonical FE basis $\{\phi_m\}_{m=1}^M$, i.e.,

$$\psi_l(\boldsymbol{x}) = \sum_{m=1}^{M} \psi_l^{(m)}\, \phi_m(\boldsymbol{x}) = \sum_{m=1}^{M} \mathbb{V}_{m,l}\, \phi_m(\boldsymbol{x}),$$

and exploiting the linearity of $g(\cdot,\cdot;\boldsymbol{\mu})$ in the second argument, yields:

$$0 = \sum_{m=1}^{M} \mathbb{V}_{m,l}\, g(u_L(\boldsymbol{\mu}), \phi_m; \boldsymbol{\mu}) = \left(\mathbb{V}^T \mathbf{G}_h(\mathbf{u}_L(\boldsymbol{\mu}); \boldsymbol{\mu})\right)_l \quad 1 \leq l \leq L,$$

where the last equality follows from the definition (4.3) of the residual vector $\mathbf{G}_h(\cdot;\boldsymbol{\mu})$ and the notation introduced in (5.2).

Then, the algebraic formulation of the reduced basis problem (5.1) can be written in compact form as:

$$\mathbf{G}_{\mathtt{rb}}(\mathbf{u}_{\mathtt{rb}}(\boldsymbol{\mu});\boldsymbol{\mu}) = \mathbb{V}^T \mathbf{G}_h(\mathbf{u}_L(\boldsymbol{\mu});\boldsymbol{\mu}) = \mathbb{V}^T \mathbf{G}_h(\mathbb{V}\,\mathbf{u}_{\mathtt{rb}}(\boldsymbol{\mu});\boldsymbol{\mu}) = \mathbf{0} \in \mathbb{R}^L. \tag{5.4}$$

This *reduced nonlinear system* imposes the orthogonality (in the Euclidean scalar product) of the residual vector $\mathbf{G}_h(\cdot;\boldsymbol{\mu})$, evaluated in $\mathbb{V}\mathbf{u}_{\mathtt{rb}}(\boldsymbol{\mu})$, to the columns of $\mathbb{V}$, thus encoding the Galerkin approach pursued at the variational level.
Finally, exploiting the chain rule and the Jacobian $\mathbb{J}_h(\cdot;\boldsymbol{\mu})$ of $\mathbf{G}_h(\cdot;\boldsymbol{\mu})$, the Jacobian $\mathbb{J}_{\mathtt{rb}}(\cdot;\boldsymbol{\mu})$ of $\mathbf{G}_{\mathtt{rb}}(\cdot;\boldsymbol{\mu})$ is given by

$$\mathbb{J}_{\mathtt{rb}}(\mathbf{w};\boldsymbol{\mu}) = \mathbb{V}^T\,\mathbb{J}_h(\mathbb{V}\,\mathbf{w};\boldsymbol{\mu})\,\mathbb{V} \in \mathbb{R}^{L\times L} \quad \forall \mathbf{w}\in\mathbb{R}^L,\ \forall\boldsymbol{\mu}\in\mathscr{P}. \tag{5.5}$$

Hence, starting from an initial guess $\mathbf{u}^0_{\mathtt{rb}} \in \mathbb{R}^L$, each iteration k, $k \geq 0$, of Newton's method applied to the reduced nonlinear system (5.4) entails the resolution of the linear system

$$\mathbb{J}_{\mathtt{rb}}(\mathbf{u}^k_{\mathtt{rb}}(\boldsymbol{\mu});\boldsymbol{\mu})\,\delta\mathbf{u}^k_{\mathtt{rb}}(\boldsymbol{\mu}) = -\mathbf{G}_{\mathtt{rb}}(\mathbf{u}^k_{\mathtt{rb}}(\boldsymbol{\mu});\boldsymbol{\mu}), \tag{5.6}$$

with $\mathbf{u}^{k+1}_{\mathtt{rb}}(\boldsymbol{\mu}) = \mathbf{u}^k_{\mathtt{rb}}(\boldsymbol{\mu}) + \delta\mathbf{u}^k_{\mathtt{rb}}(\boldsymbol{\mu})$. Therefore, applying the POD-Galerkin RB method enables a dramatic reduction of the size of the linear systems to solve whenever the dimension L of the reduced space $V_{\mathtt{rb}}$ is much lower than the dimension M of the underlying finite element space V_h.

5.1. Proper Orthogonal Decomposition

Consider a collection of N snapshots $\{u_h(\boldsymbol{\mu}^{(1)}),\dots,u_h(\boldsymbol{\mu}^{(N)})\} \subset \mathscr{M}_h$, corresponding to the finite and discrete parameter set $\Xi_N = \{\boldsymbol{\mu}^{(1)},\dots,\boldsymbol{\mu}^{(N)}\} \subset \mathscr{P}$, and let $\mathscr{M}_{\Xi_N}$ be the associated subspace, i.e.,

$$\mathscr{M}_{\Xi_N} = \operatorname{span}\{u_h(\boldsymbol{\mu}^{(1)}),\dots,u_h(\boldsymbol{\mu}^{(N)})\}.$$

Clearly, $\mathscr{M}_{\Xi_N} \subset \mathscr{M}_h$ and we can assume that $\mathscr{M}_{\Xi_N}$ provides a good approximation of $\mathscr{M}_h$, as long as the number of snapshots is sufficiently large (but typically much smaller than the dimension M of the FE space). Then, we aim at finding a parameter-independent *reduced basis* for $\mathscr{M}_{\Xi_N}$, i.e., a collection of FE functions $\{\psi_1,\dots,\psi_L\} \subset \mathscr{M}_{\Xi_N}$, with $L \ll M, N$, and L *independent* of both M and N, so that the associated linear space

$$V_{\mathtt{rb}} = \operatorname{span}\{\psi_1,\dots,\psi_L\}$$

constitutes a low-rank approximation of $\mathscr{M}_{\Xi_N}$, optimal in some later defined sense.

To this end, we work at the algebraic level. Let $\mathbf{u}_h(\boldsymbol{\mu}^{(n)}) \in \mathbb{R}^M$ be the vector collecting the degrees of freedom (with respect to the FE basis) for the n-th snapshots $u_h(\boldsymbol{\mu}^{(n)})$, $n = 1,\dots,N$, and consider the *snapshot matrix* $\mathbb{S} \in \mathbb{R}^{M\times N}$ storing such vectors in a column-wise sense, i.e.,

$$\mathbb{S} = \left[\mathbf{u}_h(\boldsymbol{\mu}^{(1)}) \,\middle|\, \dots \,\middle|\, \mathbf{u}_h(\boldsymbol{\mu}^{(N)})\right].$$

Denoting by R the rank of $\mathbb{S}$, with $R \leq \min\{M, N\}$, the singular value decomposition (SVD) of $\mathbb{S}$ ensures the existence of two orthogonal matrices $\mathbb{W} = [\mathbf{w}_1 \,|\, \dots \,|\, \mathbf{w}_M] \in \mathbb{R}^{M\times M}$ and $\mathbb{Z} = [\mathbf{z}_1 \,|\, \dots \,|\, \mathbf{z}_N] \in \mathbb{R}^{N\times N}$, and a diagonal matrix $\mathbb{D} = \operatorname{diag}(\sigma_1,\dots,\sigma_R) \in \mathbb{R}^{R\times R}$, with $\sigma_1 \geq \sigma_2 \geq \dots \geq \sigma_r > 0$, such that

$$\mathbb{S} = \mathbb{W}\begin{bmatrix}\mathbb{D} & 0\\ 0 & 0\end{bmatrix}\mathbb{Z}^T = \mathbb{W}\,\Sigma\,\mathbb{Z}^T, \tag{5.7}$$

where the zeros denote null matrices of appropriate dimensions. The real values $\{\sigma_i\}_{i=1}^R$ are called *singular values* of $\mathbb{S}$, the columns $\mathbf{w}_m \in \mathbb{R}^M$, $m = 1,\dots,M$, of $\mathbb{W}$ are called *left singular vectors* of $\mathbb{S}$, and the columns $\mathbf{z}_n \in \mathbb{R}^N$, $n = 1,\dots,N$, of $\mathbb{Z}$ are called *right singular vectors* of $\mathbb{S}$, and they are related by the following relations:

$$\begin{aligned}
&\mathbb{S}\mathbb{S}^T\mathbf{w}_m = \begin{cases}\sigma_m^2\,\mathbf{w}_m & \text{for } 1 \leq m \leq R,\\ \mathbf{0} & \text{for } R+1 \leq m \leq M,\end{cases} \qquad &&\mathbb{S}^T\mathbb{S}\,\mathbf{z}_n = \begin{cases}\sigma_n^2\,\mathbf{z}_n & \text{for } 1 \leq n \leq R,\\ \mathbf{0} & \text{for } R+1 \leq n \leq N,\end{cases}\\
&\mathbb{S}\,\mathbf{z}_i = \sigma_i\,\mathbf{w}_i \quad \text{for } 1 \leq i \leq R, &&\mathbb{S}^T\mathbf{w}_i = \sigma_i\,\mathbf{z}_i \quad \text{for } 1 \leq i \leq R.
\end{aligned} \tag{5.8}$$

Due to the sparsity pattern of Σ in (5.7), the SVD of $\mathbb{S}$ can be cast in the compact form:

$$\mathbb{S} = \mathbb{W}_R \, \mathbb{D} \, \mathbb{Z}_R^T ,$$

with $\mathbb{W}_R \in \mathbb{R}^{M \times R}$ and $\mathbb{Z}_R \in \mathbb{R}^{N \times R}$ retaining only the first R columns of W and Z, respectively, i.e.,

$$\mathbb{W}_R = \left[\mathbf{w}_1 \,\middle|\, \dots \,\middle|\, \mathbf{w}_R\right] \quad \text{and} \quad \mathbb{Z}_R = \left[\mathbf{z}_1 \,\middle|\, \dots \,\middle|\, \mathbf{z}_R\right].$$

Exploiting the orthonormality of the columns of $\mathbb{W}_R$, the generic column $\mathbf{s}_n = \mathbf{u}_h\big(\boldsymbol{\mu}^{(n)}\big)$ of $\mathbb{S}$, $n = 1, \dots N$, can be expressed as [60]

$$\mathbf{s}_n = \sum_{r=1}^{R} (\mathbf{s}_n, \mathbf{w}_r)_{\mathbb{R}^M} \mathbf{w}_r ,$$

where $(\cdot,\cdot)_{\mathbb{R}^M}$ denotes the Euclidean scalar product in $\mathbb{R}^M$. Therefore, the columns $\{\mathbf{w}_1, \dots, \mathbf{w}_R\}$ of $\mathbb{W}_R$ constitute an orthonormal basis for the column space Col($\mathbb{S}$) of $\mathbb{S}$.
Assume now we seek to approximate the columns of $\mathbb{S}$ by means of L orthonormal vectors $\{\widetilde{\mathbf{w}}_1, \dots, \widetilde{\mathbf{w}}_L\}$, with $L < R$. It is an easy matter to show that for each $\mathbf{s}_n$, $n = 1, \dots, N$, the element of span$\{\widetilde{\mathbf{w}}_1, \dots, \widetilde{\mathbf{w}}_L\}$ closest to $\mathbf{s}_n$ in the Euclidean norm $\|\cdot\|_{\mathbb{R}^M}$ is given by

$$\sum_{l=1}^{L} \big(\mathbf{s}_n, \widetilde{\mathbf{w}}_l\big)_{\mathbb{R}^M} \widetilde{\mathbf{w}}_l .$$

Hence, we could measure the error committed by approximating the columns of $\mathbb{S}$ via the vectors $\{\widetilde{\mathbf{w}}_l\}_{l=1}^{L}$ through the quantity

$$\varepsilon(\widetilde{\mathbf{w}}_1, \dots, \widetilde{\mathbf{w}}_L) = \sum_{n=1}^{N} \left\| \mathbf{s}_n - \sum_{l=1}^{L} \big(\mathbf{s}_n, \widetilde{\mathbf{w}}_l\big)_{\mathbb{R}^M} \widetilde{\mathbf{w}}_l \right\|_{\mathbb{R}^M}^2 . \tag{5.9}$$

The Schmidt-Eckart-Young theorem [18, 58] states that the *POD basis* of rank L $\{\mathbf{w}_1, \dots, \mathbf{w}_L\}$, consisting of the first L left singular values of $\mathbb{S}$, minimizes (5.9) among all the orthonormal bases of $\mathbb{R}^L$. Therefore, in the POD-Galerkin RB method, we set $\boldsymbol{\psi}_l = \mathbf{w}_l$, for all $l = 1, \dots, L$, so that

$$\mathbb{V} = \left[\mathbf{w}_1 \,\middle|\, \dots \,\middle|\, \mathbf{w}_L\right].$$

Hence, in the reduced basis problem (5.1) the test and trial functions are picked from the subspace $V_{\texttt{rb}}$ of V_h spanned by the functions $\{\psi_l\}_{l=1}^{L}$, given by

$$\psi_l(\boldsymbol{x}) = \sum_{m=1}^{M} \psi_l^{(m)} \, \phi_m(\boldsymbol{x}) = \sum_{m=1}^{M} (\mathbf{w}_l)_m \, \phi_m(\boldsymbol{x}) \quad \text{for } 1 \le l \le L. \tag{5.10}$$

From a computational viewpoint, the first L left singular vectors $\{\mathbf{w}_l\}_{l=1}^{L}$ of $\mathbb{S}$ can be efficiently computed through the so-called *method of snapshots*. We should distinguish two cases:

(a) if $M \le N$: directly solve the eigenvalue problems

$$\mathbb{S}\mathbb{S}^T \mathbf{w}_l = \lambda_l \, \mathbf{w}_l \quad \text{for } 1 \le l \le L;$$

(b) if $M > N$: compute the *correlation* matrix $\mathbb{M} = \mathbb{S}^T \mathbb{S}$ and solve the eigenvalue problems

$$\mathbb{M} \, \mathbf{z}_l = \lambda_l \, \mathbf{z}_l \quad \text{for } 1 \le l \le L.$$

Then, by (5.8) we have

$$\mathbf{w}_l = \frac{1}{\sqrt{\lambda_l}} \mathbb{S} \, \mathbf{z}_l \quad \text{for } 1 \le l \le L.$$

Algorithm 5.1 The offline and online stages for the POD-Galerkin (POD-G) RB method.

```
1: function $\mathbb{V}$ = PODG_OFFLINE($\mathscr{P}$, $\Omega_h$, $N$)
2:     generate the parameter set $\Xi_N = \{\boldsymbol{\mu}^{(1)}, \dots, \boldsymbol{\mu}^{(N)}\}$
3:     compute the high-fidelity solutions $\{\mathbf{u}_h(\boldsymbol{\mu}^{(1)}), \dots, \mathbf{u}_h(\boldsymbol{\mu}^{(N)})\}$ via FE-Newton's method
4:     generate the POD basis functions $\{\mathbf{w}_1, \dots, \mathbf{w}_L\}$ via method of snapshots
5:     assemble $\mathbb{V} = [\mathbf{w}_1 | \dots | \mathbf{w}_L]$
6: end function

1: function $\mathbf{u}_L(\boldsymbol{\mu})$ = PODG_ONLINE($\boldsymbol{\mu}$, $\mathbb{V}$)
2:     assemble and solve the reduced system (5.4) via Newton's method, yielding $\mathbf{u}_{\mathtt{rb}}(\boldsymbol{\mu})$
3:     $\mathbf{u}_L(\boldsymbol{\mu}) = \mathbb{V}\,\mathbf{u}_{\mathtt{rb}}(\boldsymbol{\mu})$
4: end function
```

5.2. *Implementation: details and issues*

The numerical procedure presented so far can be efficiently carried out within an offline-online framework [51]. The parameter-independent *offline* step consists of the generation of the snapshots through a high-fidelity, expensive discretization scheme and the subsequent construction of the reduced basis via POD. To determine an appropriate dimension for the basis, which ensures a desired degree of accuracy, one can resort to empirical criteria, like, e.g., the *relative information content* [53]. Then, given a new parameter value $\boldsymbol{\mu} \in \mathscr{P}$, the nonlinear reduced system (5.4) is solved *online* using, e.g., Newton's method, which entails the assembly and resolution of linear systems of the form (5.6). The main steps of the resulting POD-Galerkin (POD-G) RB method are summarized in Algorithm 5.1.

However, to enjoy a significant reduction in the computational burden with respect to traditional (full-order) discretization techniques, the complexity of any online query should be *independent* of the original size of the problem. At this regard, notice that the operative definitions (5.4) and (5.5) of the reduced residual vector $\mathbf{G}_{\mathtt{rb}}(\cdot;\boldsymbol{\mu})$ and its Jacobian $\mathbb{J}_{\mathtt{rb}}(\cdot;\boldsymbol{\mu})$ involve the evaluation of the (high-fidelity) residual vector $\mathbf{G}_h(\cdot;\boldsymbol{\mu})$ and its Jacobian $\mathbb{J}_h(\cdot;\boldsymbol{\mu})$, whose cost clearly dependens on M. Moreover, due to the nonlinearity of the underlying PDE and the non-affinity in the parameter dependence (partially induced by the transformation map $\boldsymbol{\Phi}(\cdot;\boldsymbol{\mu})$), the assembly of the reduced linear systems (5.6) has to be embodied directly in the online stage, thus seriously compromising the efficiency of the overall procedure [3]. Without escaping the algebraic framework, this can be successfully overcome upon resorting to suitable techniques such as the discrete empirical interpolation method (DEIM) [10] or its matrix variant (MDEIM) [49], aiming at recovering an affine dependency on the parameter $\boldsymbol{\mu}$. On the other hand, we should point out that the implementation of such techniques is problem dependent and of an *intrusive* nature, as it requires to access and modify the assembly routines of the corresponding computational code [9]. Moreover, any interpolation procedure unavoidably introduces a further level of approximation. As a matter of fact, typically one needs to generate a larger number of snapshots in the offline stage and then retain a larger number of POD modes to guarantee the same accuracy provided by the standard POD-Galerkin method [3].

6. A non-intrusive reduced basis method using artificial neural networks

The scenario portrayed so far motivates the research for an alternative approach to tackle any online query within the reduced basis framework, hopefully skipping the assembly and resolution of the reduced system. To this end, let us remark that there exists a one-to-one correspondence between the reduced space $V_{\mathtt{rb}}$ and the column space Col($\mathbb{V}$) of $\mathbb{V}$. Indeed, letting $\{\phi_1, \dots, \phi_M\}$ be a basis for V_h and $\{\psi_1, \dots, \psi_L\}$ be the reduced basis, from Eq. (5.10) follows:

$$V_{\mathtt{rb}} \ni v_L = \sum_{j=1}^{L} v_{\mathtt{rb}}^{(j)}\, \psi_j = \sum_{j=1}^{L} v_{\mathtt{rb}}^{(j)} \sum_{i=1}^{M} \mathbb{V}_{i,j}\, \phi_i = \sum_{i=1}^{M} \left(\mathbb{V}\,\mathbf{v}_{\mathtt{rb}}\right)_i \phi_i \quad \leftrightarrow \quad \mathbb{V}\,\mathbf{v}_{\mathtt{rb}} \in \mathrm{Col}(\mathbb{V})\,.$$

In particular, this implies that the projection of any $v_h \in V_h$ onto $V_{\mathtt{rb}}$ in the discrete scalar product $(\cdot,\cdot)_h$,

$$(\chi_h, \xi_h)_h = \sum_{i=1}^{M} \chi_h^{(i)}\, \xi_h^{(i)} = (\boldsymbol{\chi}_h, \boldsymbol{\xi}_h)_{\mathbb{R}^M} \quad \forall \chi_h, \xi_h \in V_h\,, \tag{6.1}$$

algebraically corresponds to the projection $\mathbf{v}_h^{\mathbb{V}}$ of $\mathbf{v}_h$ onto $\mathrm{Col}(\mathbb{V})$ in the Euclidean scalar product, given by

$$\mathbf{v}_h^{\mathbb{V}} = \mathbb{P}\,\mathbf{v}_h \qquad \text{with} \qquad \mathbb{P} = \mathbb{V}\mathbb{V}^T \in \mathbb{R}^{M\times M} .$$

Note that $\mathbf{v}_h^{\mathbb{V}}$ is the element of $\mathrm{Col}(\mathbb{V})$ closest to $\mathbf{v}_h$ in the Euclidean norm, i.e.,

$$\left\| \mathbf{v}_h - \mathbf{v}_h^{\mathbb{V}} \right\|_{\mathbb{R}^M} = \inf_{\mathbf{w}_h \in \mathrm{Col}(\mathbb{V})} \left\| \mathbf{v}_h - \mathbf{w}_h \right\|_{\mathbb{R}^M} .$$

Therefore, the element of $V_{\mathtt{rb}}$ closest to the high-fidelity solution u_h in the discrete norm $\|\cdot\|_h = \sqrt{(\cdot,\cdot)_h}$ can be expressed as

$$u_h^{\mathbb{V}}(\boldsymbol{x};\boldsymbol{\mu}) = \sum_{j=1}^{M} \left(\mathbb{V}\mathbb{V}^T \mathbf{u}_h(\boldsymbol{\mu})\right)_j \phi_j(\boldsymbol{x}) = \sum_{i=1}^{L} \left(\mathbb{V}^T \mathbf{u}_h(\boldsymbol{\mu})\right)_i \psi_i(\boldsymbol{x}) .$$

Motivated by this last equality, once a reduced basis has been constructed (e.g., via POD of the snapshot matrix), we aim at approximating the function

$$\begin{aligned} \boldsymbol{\pi} \, : \, \mathscr{P} \subset \mathbb{R}^P \; &\to \; \mathbb{R}^L \\ \boldsymbol{\mu} \; &\mapsto \; \mathbb{V}^T \mathbf{u}_h(\boldsymbol{\mu}) , \end{aligned} \tag{6.2}$$

which maps each input vector parameter $\boldsymbol{\mu} \in \mathscr{P}$ to the coefficients $\mathbb{V}^T \mathbf{u}_h(\boldsymbol{\mu})$ for the expansion of $u_h^{\mathbb{V}}$ in the reduced basis $\{\psi_i\}_{i=1}^L$. Then, given a new parameter instance $\boldsymbol{\mu}$, the associated RB solution is simply given by the evaluation in $\boldsymbol{\mu}$ of the approximation $\hat{\boldsymbol{\pi}}$ of $\boldsymbol{\pi}$, i.e.

$$\mathbf{u}_{\mathtt{rb}}(\boldsymbol{\mu}) = \hat{\boldsymbol{\pi}}(\boldsymbol{\mu}) ,$$

and, consequently,

$$\mathbf{u}_L(\boldsymbol{\mu}) = \mathbb{V}\, \hat{\boldsymbol{\pi}}(\boldsymbol{\mu}) .$$

Note that, provided that the construction of $\hat{\boldsymbol{\pi}}$ is entirely carried out within the offline stage, this approach leads to a *non-intrusive* RB method, enabling a complete decoupling between the online step and the underlying full-order model. Moreover, the accuracy of the resulting reduced solution uniquely relies on the quality of the reduced basis and the effectiveness of the approximation $\hat{\boldsymbol{\pi}}$ of the map $\boldsymbol{\pi}$.

In the literature, different approaches for the *interpolation* of (6.2) have been developed, e.g., exploiting some geometrical considerations concerning the solution manifold $\mathscr{M}$ [1], or employing radial basis functions [12]. In this work we resort to artificial neural networks, in particular multi-layer perceptrons, for the *nonlinear regression* of the map $\boldsymbol{\pi}$, leading to the POD-NN RB method. As described in Subsection 2.3, any neural network is tailored to the particular application at hand by means of a preliminary *training* phase. Here, we are concerned with a function regression task, thus we straightforwardly adopt a *supervised learning* paradigm, training the perceptron via exposition to a collection of (known) input-output pairs

$$P_{tr} = \left\{ \left(\boldsymbol{\mu}^{(i)}, \mathbb{V}^T \mathbf{u}_h\big(\boldsymbol{\mu}^{(i)}\big) \right) \right\}_{i=1}^{N_{tr}} .$$

According to the notation and nomenclature introduced previously, for $i = 1, \ldots, N_{tr}$, $\mathbf{p}_i = \boldsymbol{\mu}^{(i)} \in \mathbb{R}^P$ represents the *input pattern* and $\mathbf{t}_i = \mathbb{V}^T \mathbf{u}_h\big(\boldsymbol{\mu}^{(i)}\big) \in \mathbb{R}^L$ the associated *teaching input*; together, they constitute a *training pattern*. In this respect, note that the teaching inputs $\mathbb{V}^T \mathbf{u}_h\big(\boldsymbol{\mu}^{(i)}\big)$, $i = 1, \ldots, N_{tr}$, are generated through the FE solver. On the one hand, this ensures the reliability of the teaching patterns, given the assumed high-fidelity of the FE scheme On the other hand, this also suggests to incorporate the learning phase of the perceptron within the offline step of the POD-NN RB method, as described in Algorithm 6.1. In doing so, we exploit the natural decoupling between the training and the evaluation of neural networks, thus fulfilling the necessary requirement to enable great online efficiency.

However, it should be pointed out that the design of an effective learning procedure may require a larger amount of snapshots than the generation of the reduced space does. Moreover, we mentioned in Section 2 the time-consuming yet unavoidable *trial-and-error* approach which one should pursue in the search for an optimal network topology. To this end, we propose an automatic procedure, resumed in the following.

Algorithm 6.1 The offline and online stages for the POD-NN RB method.

```
1: function $[\mathbb{V}, \mathscr{N}_{\texttt{rb}}, \mathscr{V}_{\texttt{rb}}, \mathbf{w}_{\texttt{rb}}]$ = PODNN_OFFLINE($\mathscr{P}$, $\Omega_h$, $N$)
2:     generate the parameter set $\Xi_N = \{\boldsymbol{\mu}^{(1)}, \dots, \boldsymbol{\mu}^{(N)}\}$
3:     compute the high-fidelity solutions $\{\mathbf{u}_h(\boldsymbol{\mu}^{(1)}), \dots, \mathbf{u}_h(\boldsymbol{\mu}^{(N)})\}$ via FE-Newton's method
4:     generate the POD basis functions $\{\mathbf{w}_1, \dots, \mathbf{w}_L\}$ via method of snapshots
5:     assemble $\mathbb{V} = [\mathbf{w}_1 \,|\, \dots \,|\, \mathbf{w}_L]$
6:     find an optimal network configuration $(\mathscr{N}_{\texttt{rb}}, \mathscr{V}_{\texttt{rb}}, \mathbf{w}_{\texttt{rb}})$ relying upon LHS and Levenberg-Marquardt algorithm
7: end function

1: function $\mathbf{u}_L^{\texttt{NN}}(\boldsymbol{\mu})$ = PODNN_ONLINE($\boldsymbol{\mu}$, $\mathbb{V}$, $\mathscr{N}_{\texttt{rb}}$, $\mathscr{V}_{\texttt{rb}}$, $\mathbf{w}_{\texttt{rb}}$)
2:     evaluate the output $\mathbf{u}_{\texttt{rb}}^{\texttt{NN}}(\boldsymbol{\mu})$ of the network $(\mathscr{N}_{\texttt{rb}}, \mathscr{V}_{\texttt{rb}}, \mathbf{w}_{\texttt{rb}})$ for the input vector $\boldsymbol{\mu}$
3:     $\mathbf{u}_L^{\texttt{NN}}(\boldsymbol{\mu}) = \mathbb{V}\,\mathbf{u}_{\texttt{rb}}^{\texttt{NN}}(\boldsymbol{\mu})$
4: end function
```

While the Cybenko's theorems (see Subsection 2.2) allows one to consider perceptrons with no more than two hidden layers, no similar a priori and general results are available for the number H of neurons per layer (to ease the work, we uniquely consider networks with the same number of neurons in both the first and the second hidden layer). Hence, given an initial amount N_{tr} of training samples (say $N_{tr} = 100$), we train the network for increasing values of H, stopping when overfitting of training data occurs (due to an excessive number of neurons with respect to the number of training patterns). In case the best configuration, i.e., the one yielding the smallest error on a test data set, does not meet a desired level of accuracy, we generate a new set of snapshots, which will enlarge the current training set, and we then proceed to re-train the networks. At this point, it is worth pointing out two remarks.

(i) Once the training set has been enriched, we can limit ourselves to network configurations including a number of neurons *non-smaller* than the current optimal network does. Indeed, the error (on the test data set) yielded by a neural network is decreasing in the number of patterns it is exposed to during the learning phase, and the larger the number of neurons, the faster the decay.

(ii) In order to maximize the additional quantity of information available for the learning, we should ensure that the new training inputs, i.e., parameter values, do not overlap with the ones already present in the training parameter set. To this aim, we pursue an euristhic approach, employing, at each iteration, the latin hypercube sampling [33], which has proved to provide a good compromise between randomness and even covarage of the parameter domain.

The procedure is then iterated until a satisfactory degree of accuracy and generalization is attained, or the maximum number of training patterns is reached. Therefore, the speed up enabled by the pursuit of a neural network-based approach to tackle any *online* query comes at the cost of an extended *offline* phase.

In our numerical tests, we resort to the Levenberg-Marquardt algorithm to properly adjust the weights of the perceptron during the learning phase, relying on the mean squared error (MSE) (2.2) as performance function. To motivate this choice, let

$$\mathbf{u}_{\texttt{rb}}^{\texttt{NN}}(\boldsymbol{\mu}) \in \mathbb{R}^L$$

be the (actual) output provided by the network for a given input $\boldsymbol{\mu}$, and

$$\mathbf{u}_L^{\texttt{NN}}(\boldsymbol{\mu}) = \mathbb{V}\, \mathbf{u}_{\texttt{rb}}^{\texttt{NN}}(\boldsymbol{\mu}) \in \text{Col}(\mathbb{V}) \subset \mathbb{R}^M .$$

Then (omitting the dependence on the input vector to ease the notation):

$$MSE\big(\mathbf{u}_{\texttt{rb}}^{\texttt{NN}}, \mathbb{V}^T\mathbf{u}_h\big) \propto \big\|\mathbf{u}_{\texttt{rb}}^{\texttt{NN}} - \mathbb{V}^T\mathbf{u}_h\big\|_{\mathbb{R}^L}^2 = \big\|\mathbf{u}_L^{\texttt{NN}} - \mathbb{V}\,\mathbb{V}^T\mathbf{u}_h\big\|_{\mathbb{R}^M}^2 = \big\|u_L^{\texttt{NN}} - u_h^{\mathbb{V}}\big\|_h^2 ,$$

where

$$u_L^{\texttt{NN}}(\boldsymbol{x}; \boldsymbol{\mu}) = \sum_{i=1}^{L} \big(\mathbf{u}_{\texttt{rb}}^{\texttt{NN}}(\boldsymbol{\mu})\big)_i \, \psi_i(\boldsymbol{x}) \in V_{\texttt{rb}} .$$

Therefore, by minimizing the MSE, we actually minimize the distance (in the discrete norm $\|\cdot\|_h$) between the approximation provided by the neural network and the projection of the FE solution onto the reduced space $V_{\texttt{rb}}$ for all the training inputs

$\boldsymbol{\mu}^{(i)}$, $i = 1, \dots, N_{tr}$. The proper *generalization* to other parameter instances not included in the training set is then ensured by the implementation of suitable techniques (e.g., early stopping [43], generalized cross validation [36]) aiming at preventing the network to *overfit* the training data.

7. Numerical results

In this section, we present the numerical results obtained via the POD-G and the POD-NN RB methods applied to parametrized full-Dirichlet boundary value problems (BVPs) for the nonlinear Poisson equation and the incompressible steady Navier-Stokes equations. We consider instances of the Poisson equation stated on either one- or two-dimensional domains. In the one-dimensional case, we deal uniquely with physical parameters, which address the diffusion coefficient, the source term or the boundary conditions; whereas, in two spatial dimensions we only consider parameters which affect the shape of the domain. For the two-dimensional Navier-Stokes equations we also consider a purely geometrical parametrization.

The two RB techniques considered in this work are compared both in terms of accuracy and performance enabled at the online stage. For this, let $\|\cdot\|$ be the canonical (Euclidean) norm on $\mathbb{R}^M$. In the online phases of the POD-G and POD-NN methods, for a new parameter value $\boldsymbol{\mu} \in \mathscr{P}$ (not involved either in the generation of the POD basis nor in the identification of optimal neural network), the following *relative* errors with respect to the high-fidelity solution $\mathbf{u}_h(\boldsymbol{\mu})$ are analyzed:

(a) the POD-G relative error,

$$\varepsilon_{\texttt{PODG}}(L, \boldsymbol{\mu}) = \frac{\left\|\mathbf{u}_h(\boldsymbol{\mu}) - \mathbf{u}_L(\boldsymbol{\mu})\right\|}{\left\|\mathbf{u}_h(\boldsymbol{\mu})\right\|} = \frac{\left\|\mathbf{u}_h(\boldsymbol{\mu}) - \mathbb{V}\,\mathbf{u}_{\texttt{rb}}(\boldsymbol{\mu})\right\|}{\left\|\mathbf{u}_h(\boldsymbol{\mu})\right\|}; \tag{7.1}$$

(b) the POD-NN relative error,

$$\varepsilon_{\texttt{PODNN}}(L, \boldsymbol{\mu}) = \frac{\left\|\mathbf{u}_h(\boldsymbol{\mu}) - \mathbf{u}_L^{\texttt{NN}}(\boldsymbol{\mu})\right\|}{\left\|\mathbf{u}_h(\boldsymbol{\mu})\right\|} = \frac{\left\|\mathbf{u}_h(\boldsymbol{\mu}) - \mathbb{V}\,\mathbf{u}_{\texttt{rb}}^{\texttt{NN}}(\boldsymbol{\mu})\right\|}{\left\|\mathbf{u}_h(\boldsymbol{\mu})\right\|}; \tag{7.2}$$

(c) the relative projection error, i.e., the error committed by approximating the high-fidelity solution with its projection (in the discrete scalar product $(\cdot,\cdot)_h$, see (6.1)) onto the reduced space $V_{\texttt{rb}}$,

$$\varepsilon_{\mathbb{V}}(L, \boldsymbol{\mu}) = \frac{\left\|\mathbf{u}_h(\boldsymbol{\mu}) - \mathbf{u}_h^{\mathbb{V}}(\boldsymbol{\mu})\right\|}{\left\|\mathbf{u}_h(\boldsymbol{\mu})\right\|} = \frac{\left\|\mathbf{u}_h(\boldsymbol{\mu}) - \mathbb{V}\mathbb{V}^T\mathbf{u}_h(\boldsymbol{\mu})\right\|}{\left\|\mathbf{u}_h(\boldsymbol{\mu})\right\|}; \tag{7.3}$$

recall that (7.3) provides a lower-bound for both (7.1) and (7.2) (as explained in Section 6.

The above errors are then evaluated on a test parameter set $\Xi_{te} \subset \mathscr{P}$ consisting of N_{te} randomly picked samples. Given that a sufficiently large number of test values is chosen, statistics for $\varepsilon_{\texttt{PODG}}(L,\cdot)$, $\varepsilon_{\texttt{PODNN}}(L,\cdot)$ and $\varepsilon_{\mathbb{V}}(L,\cdot)$ on Ξ_{te} can be reasonably assumed independent of the particular choice made for Ξ_{te}, thus making any subsequent error analysis reliable. In particular, in our numerical studies we let N_{te} range from 50 up to 100, and we consider the average of the errors over the test data set, respectively denoted by

$$\bar{\varepsilon}_{\texttt{PODG}} = \bar{\varepsilon}_{\texttt{PODG}}(L) = \frac{\sum_{\boldsymbol{\mu}\in\Xi_{te}} \varepsilon_{\texttt{PODG}}(L,\boldsymbol{\mu})}{N_{te}}, \qquad \bar{\varepsilon}_{\texttt{PODNN}} = \bar{\varepsilon}_{\texttt{PODNN}}(L) = \frac{\sum_{\boldsymbol{\mu}\in\Xi_{te}} \varepsilon_{\texttt{PODNN}}(L,\boldsymbol{\mu})}{N_{te}}, \qquad \bar{\varepsilon}_{\mathbb{V}} = \bar{\varepsilon}_{\mathbb{V}}(L) = \frac{\sum_{\boldsymbol{\mu}\in\Xi_{te}} \varepsilon_{\mathbb{V}}(L,\boldsymbol{\mu})}{N_{te}}.$$

In the training phase of neural networks, we rely upon the well-known cross-validation procedure [36]. While the training samples $\Xi_{tr} \subset \mathscr{P}$ are generated via successive latin hypercube samplings, the *validation* inputs $\Xi_{va} \subset \mathscr{P}$ are randomly picked through a Monte Carlo sampling, as it is done for Ξ_{te}. The ratio between the size of Ξ_{va} and Ξ_{tr} is set to 0.3. The training is then performed using the *multiple restarts* approach to prevent the results to depend on the way the weights are (randomly) initialized; see, e.g., [38, 43]. Typically, five restarts are performed for each network topology. To ease the research for an optimal network configuration and by exploiting Cybenko's results (see Subsection 2.2), we limit ourselves to three-layers neural networks, with the same number of neurons for both hidden layers. For each topology, the hyperbolic tangent is used as activation function for the hidden neurons.

All the results presented in the following subsections have been obtained via a MATLAB® implementation of the FE, POD-G and POD-NN methods, with all the simulations carried out on a Lenovo laptop equipped with a CPU Intel Core i7 @ 2.50 GHz

7.1. *One-dimensional Poisson equation*

Consider the following BVP for the one-dimensional Poisson equation, featuring an exponential nonlinearity (in the diffusion coefficient) and involving three parameters:

$$\begin{cases} -\big(\exp(u(\boldsymbol{\mu}))\, u(\boldsymbol{\mu})'\big)' = s(x;\boldsymbol{\mu}) \quad \text{in } \Omega = \left(-\dfrac{\pi}{2}, \dfrac{\pi}{2}\right), \\ u(\boldsymbol{\mu})\big|_{x=\pm\pi/2} = \mu_2 \left(2 \pm \sin\left(\dfrac{\mu_1 \pi}{2}\right)\right) \exp\left(\pm\dfrac{\mu_3 \pi}{2}\right). \end{cases} \tag{7.4}$$

Here, $\boldsymbol{\mu} = (\mu_1, \mu_2, \mu_3) \in \mathscr{P} = [1,3] \times [1,3] \times [-0.5, 0.5]$ and $s(\cdot;\boldsymbol{\mu})$ is defined such that $u_{ex}(x;\boldsymbol{\mu}) = \mu_2 (2 + \sin(\mu_1 x)) \exp(\mu_3 x)$ is the exact solution to the problem for any $\boldsymbol{\mu} \in \mathscr{P}$.

The left plot of Fig. 7.1 shows the exponential convergence of the POD-G and POD-NN solutions with respect to the number of basis functions L retained in the model. For the POD-NN method, results refer to different amounts of training patterns and hidden neurons. First, note that including $L = 10$ POD modes within the reduced basis framework, both numerical procedures enable an average relative error of about 10^{-5} on a test set Ξ_{te} of $N_{te} = 100$ randomly chosen samples. However, when only a few modes are considered (e.g., $L \leq 5$), the POD-NN scheme may lead to a significant reduction of the error with respect to the POD-G technique. Moreover, as we expand the training set, we obtain more accurate predictions for a larger number of POD coefficients, provided that we allow the size of the network to properly increase. The reliability of the proposed RB method is also confirmed by the right plot of Fig. 7.1, providing a comparison between the FE and POD-NN solutions for some parameter values.

Diving deeplier into the analysis of the POD-NN method, Fig. 7.2 offers the results concerning the search for an optimal three-layers network configuration using the methodology described in Section 6. The steps followed by the routine are represented by solid tracts. However, for the sake of completeness, we also report the test error (i.e., the minimum over multiple restarts) for any considered number of hidden neurons per layer (H_1 and H_2) and any dimension of the training set (N_{tr}). We remark that the basic assumption which the proposed routine relies on is fulfilled: as the number of available samples increases, the amount of neurons which allows to attain the minimum error increases as well, while the minimum error itself decreases.

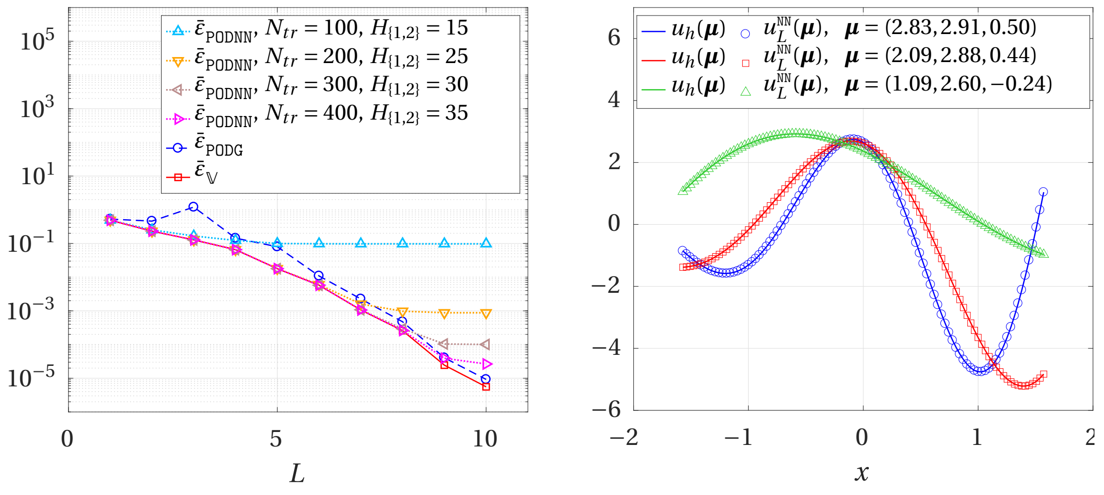

Figure 7.1. Convergence analysis for the POD-G and POD-NN methods applied to problem (7.4) (*left*) and comparison between the FE and the POD-NN solutions for three parameter values (*right*). These latter results have been obtained via a neural network with $H_1 = H_2 = 35$ units per hidden layer, and employing $L = 10$ POD modes.

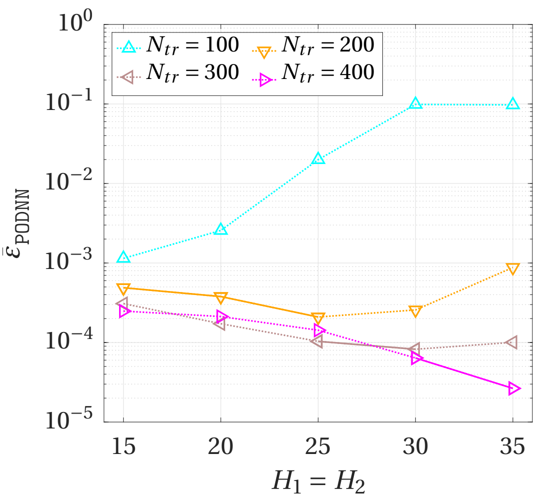

Figure 7.2. Error analysis for the POD-NN RB method applied to problem (7.4) for several numbers of training samples. The solid sections represent the steps followed by the automatic routine desscribed in Section 6.

7.2. Two-dimensional Poisson equation

Let $\boldsymbol{\mu} = [\mu_1, \mu_2, \mu_3] \in \mathscr{P} = [-0.5, 0.5] \times [-0.5, 0.5] \times [1, 5]$ and $\widetilde{\Omega}(\boldsymbol{\mu})$ be the stenosis geometry reported on the left in Fig. 7.3, parametrized in the depths μ_1 and μ_2 of the bottom and top restrictions (or inflations), respectively, and the length μ_3 of the vessel. The Poisson problem we deal with in this section reads:

$$\begin{cases} -\widetilde{\nabla} \cdot \left(\exp(\widetilde{u}(\boldsymbol{\mu}))\, \widetilde{\nabla} \widetilde{u}(\boldsymbol{\mu}) \right) = \widetilde{s}(\widetilde{x}, \widetilde{y}) & \text{in } \widetilde{\Omega}(\boldsymbol{\mu}) \,, \\ \widetilde{u}(\boldsymbol{\mu}) = \widetilde{\sigma}_x \sin(\pi \widetilde{\sigma}_x) \cos(\pi \widetilde{\sigma}_y) & \text{on } \partial\widetilde{\Omega}(\boldsymbol{\mu}) \,. \end{cases} \tag{7.5}$$

with the source term $\widetilde{s} = \widetilde{s}(\widetilde{x}, \widetilde{y})$ properly chosen so that the exact solution to the problem is given by
$\widetilde{u}_{ex}(\widetilde{x}, \widetilde{y}) = \widetilde{y} \sin(\pi \widetilde{x}) \cos(\pi \widetilde{y})$ for all $\boldsymbol{\mu} \in \mathscr{P}$. Albeit the state equation shows up an exponential nonlinearity and the computational domain presents curvilinear boundaries, both the RB methodologies studied in this work provide accurate solutions, close to the optimal one, i.e., $u_h^{\mathbb{V}}(\boldsymbol{\mu})$. This can be drawn from Fig. 7.4, offering the finite element solution (*top left*) to (**??**) when $\boldsymbol{\mu} = (0.349, -0.413, 4.257)$, and the pointwise errors committed by either the projection onto $V_{\mathtt{rb}}$ (*top right*), or the POD-G method (*bottom left*), or the POD-NN method (*bottom right*). The computational mesh employed consists of 2792 nodes, resulting in $M = 2632$ degrees of freedom (as many as the inner nodes) for the FE scheme. The reduced

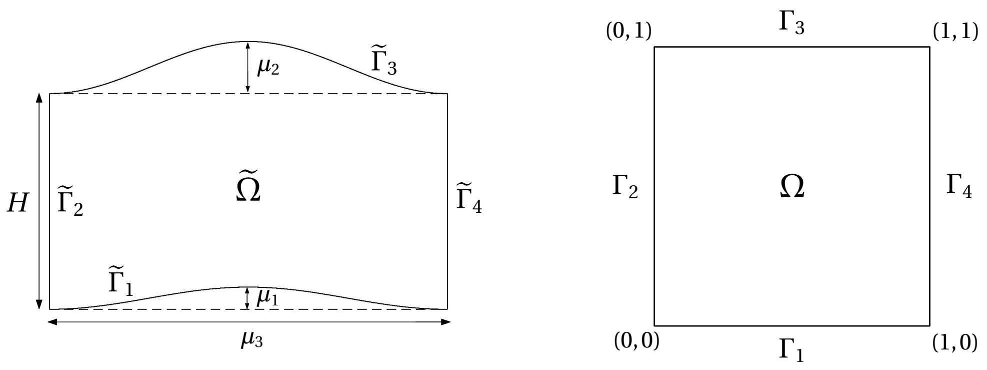

Figure 7.3. The physical (*left*) and reference (*right*) domains for the Poisson problem (7.5).

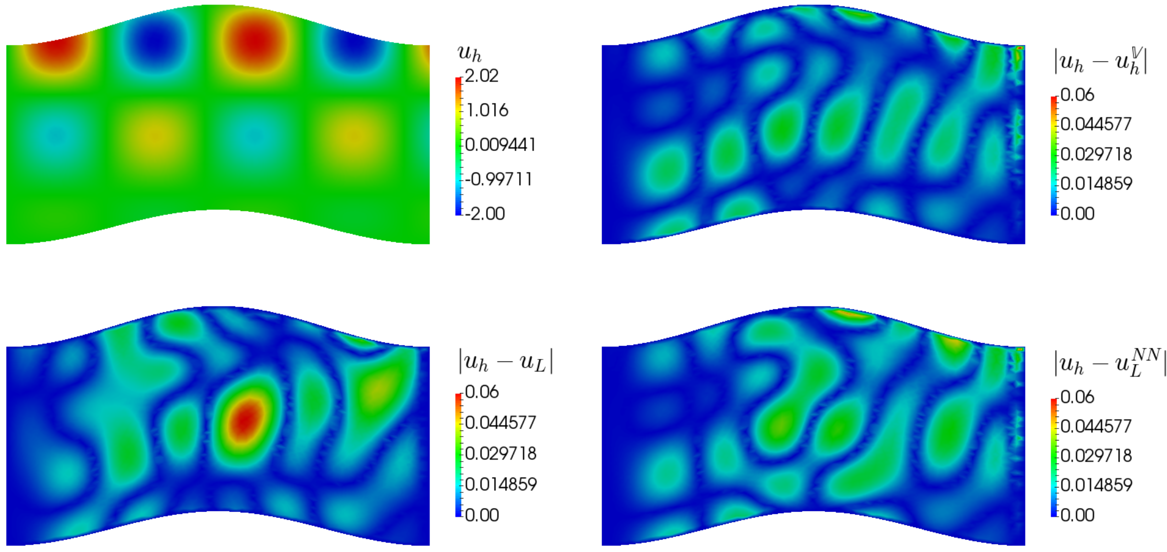

Figure 7.4. FE solution (*top left*) to the Poisson problem (7.5) with $\boldsymbol{\mu} = (0.349, -0.413, 4.257)$, and pointwise errors yielded by either its projection onto $V_{\mathtt{rb}}$ (*top right*), or the POD-G method (*bottom left*), or the POD-NN method (*bottom right*). The results have been obtained by employing $L = 30$ POD modes.

space $V_{\mathtt{rb}}$ is generated by $L = 30$ basis functions, given by POD of $N = 100$ snapshots. Specifically, the results concerning the POD-NN method have been obtained by employing a neural network equipped with $H_1 = H_2 = 35$ neurons per hidden layer and trained with $N_{tr} = 200$ learning samples. In this way, the POD-NN procedure leads to an error field which shows similar patterns to those featured by the projection error field. This is not surprising, due to the way neural networks are trained within the POD-NN framework (see Section 6).

A quantitative evidence of the efficacy of the RB approximations is given in the plot on the left in Fig. 7.5, which reports a convergence analysis for both the POD-G and the POD-NN methods with respect to the number L of retained modal basis functions. As usual, the error has to be intended as an average over a parameter data set Ξ_{te}, here consisting of $N_{te} = 50$ samples. However, the second plot of Fig. 7.5 reveals how the former scheme produces a response for any online query approximately 10^3 times slowlier than the proposed POD-NN procedure does, preventing any computational gain with respect to the finite element scheme.

Let us further analyze the first plot of Fig. 7.5. Within the POD-NN framework, when the proper orthogonal decomposition of a set of $N = 100$ snapshots is coupled with a three-layers perceptron with 35 neurons per hidden layer, trained to approximate the map (6.2) relying on $N_{tr} = 200$ learning patterns, for each $L \leq 30$ the relative error is smaller than the error committed by the POD-Galerkin procedure. Yet, halfing the number of learning patterns employed, the POD-NN error curve stops decreasing at $L = 20$, then incurring in a plateu. In this regard, Fig. 7.6 suggests that as the size of the available training set decreases, one should coherently reduce the amount of computing units to be embodied in the network, thus to limit the risk of overfitting.

The distinguishing and novel feature of the POD-NN method is represented by the employment of multi-layer perceptrons to recover the coefficients of the reduced model. To motivate this choice, let us pursue a more traditional approach in the interpolation step by resorting to cubic splines [15]. To this end, let $\Xi_\delta \subset \mathscr{P}$ be a tensor-product grid on the parameter domain, based on, e.g., Chebyshev nodes. In the offline phase, for each $\boldsymbol{\mu}_\delta \in \Xi_\delta$, we compute the truth solution $\mathbf{u}_h(\boldsymbol{\mu}_\delta) \in \mathbb{R}^M$ and we extract the expansion coefficients $\mathbb{V}^T \mathbf{u}_h(\boldsymbol{\mu}_\delta) \in \mathbb{R}^L$. At the online stage, given a new parameter value $\boldsymbol{\mu} \in \mathscr{P}$, the i-th expansion coefficient, $i = 1, \dots, L$, is sought by cubic spline interpolation of the samples

$$\left\{\left(\boldsymbol{\mu}_\delta, \left(\mathbb{V}^T \mathbf{u}_h(\boldsymbol{\mu}_\delta)\right)_i\right)\right\}_{\boldsymbol{\mu}_\delta \in \Xi_\delta}.$$

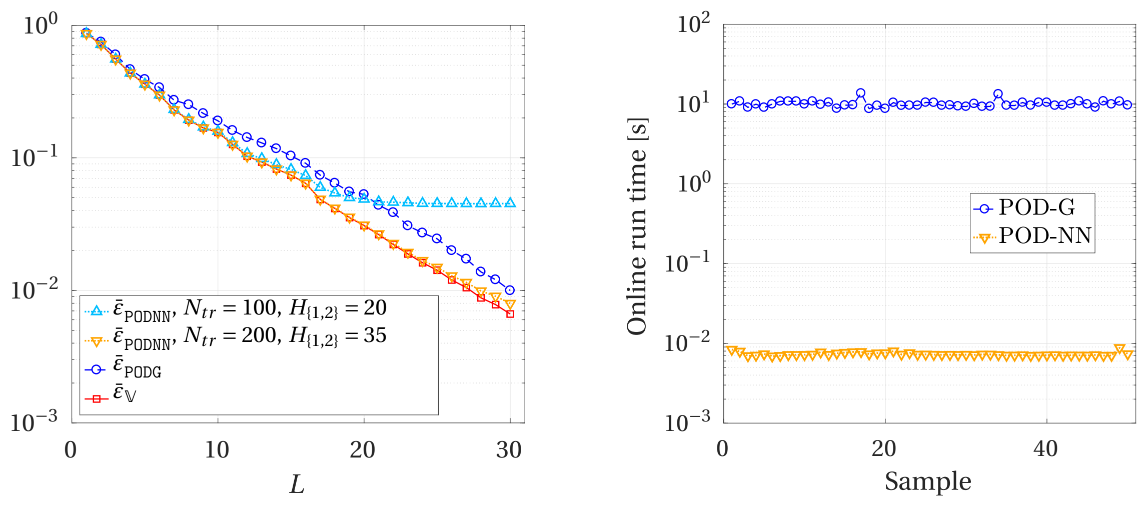

Figure 7.5. Error analysis (*left*) and online CPU time (*right*) for the POD-G and the POD-NN methods applied to problem (7.5). $N_{te} = 50$ randomly picked parameter values are considered. The reduced basis have been generated via POD, relying on $N = 100$ snapshots. The second plot refers to RB models including $L = 30$ modal functions; within the POD-NN framework, a neural network emboding 35 neurons per inner layer has been used.

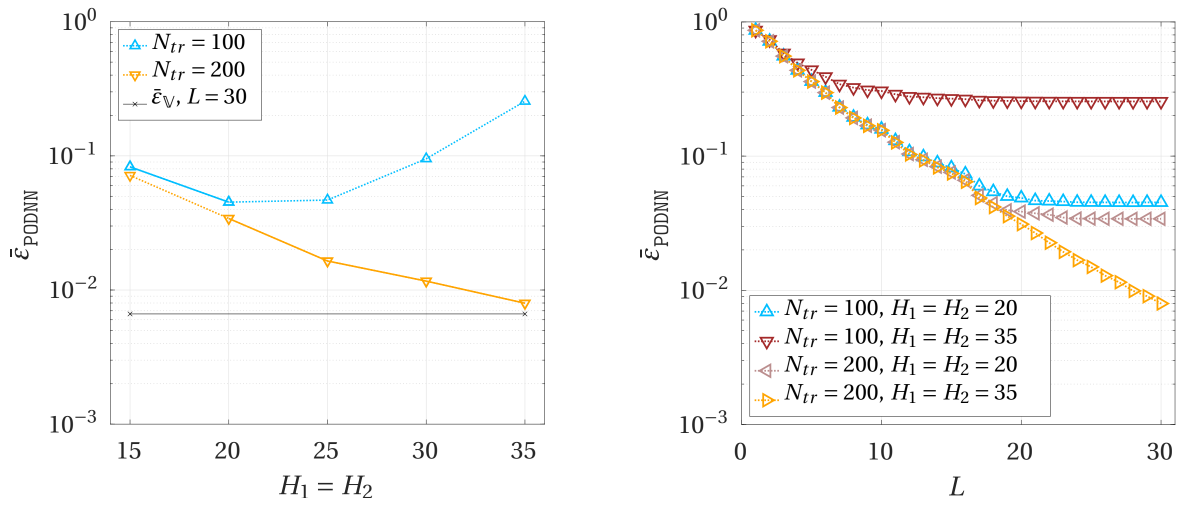

Figure 7.6. Convergence analysis with respect to the number of hidden neurons (*left*) and modal functions (*right*) used within the POD-NN framework applied to problem (7.5). The results provided in the first plot have been obtained using $L = 30$ modes; the solid tracts refer to the steps performed by the automatic routine carried out to find an optimal network configuration.

Hence, denoting by $\mathbf{u}_{\mathtt{rb}}^{\mathtt{CS}}(\boldsymbol{\mu}) \in \mathbb{R}^L$ the so-constructed approximation of $\mathbb{V}^T \mathbf{u}_h(\boldsymbol{\mu})$, the reduced-order approximation of $\mathbf{u}_h(\boldsymbol{\mu})$ is given by $\mathbf{u}_L^{\mathtt{CS}}(\boldsymbol{\mu}) = \mathbb{V}\mathbf{u}_{\mathtt{rb}}^{\mathtt{CS}}(\boldsymbol{\mu})$. Similarly to the POD-G and the POD-NN method, the accuracy of the resulting POD-CS procedure can be assessed by evaluating the relative error $\varepsilon_{\mathtt{PODCS}}(L, \boldsymbol{\mu})$, defined as

$$\varepsilon_{\mathtt{PODCS}}(L, \boldsymbol{\mu}) = \frac{\left\| \mathbf{u}_h(\boldsymbol{\mu}) - \mathbf{u}_L^{\mathtt{CS}}(\boldsymbol{\mu}) \right\|}{\left\| \mathbf{u}_h(\boldsymbol{\mu}) \right\|} = \frac{\left\| \mathbf{u}_h(\boldsymbol{\mu}) - \mathbb{V}\mathbf{u}_{\mathtt{rb}}^{\mathtt{CS}}(\boldsymbol{\mu}) \right\|}{\left\| \mathbf{u}_h(\boldsymbol{\mu}) \right\|},$$

on a test parameter set $\Xi_{te} \subset \mathscr{P}$, with $\Xi_{te} \cap \Xi_\delta = \emptyset$.

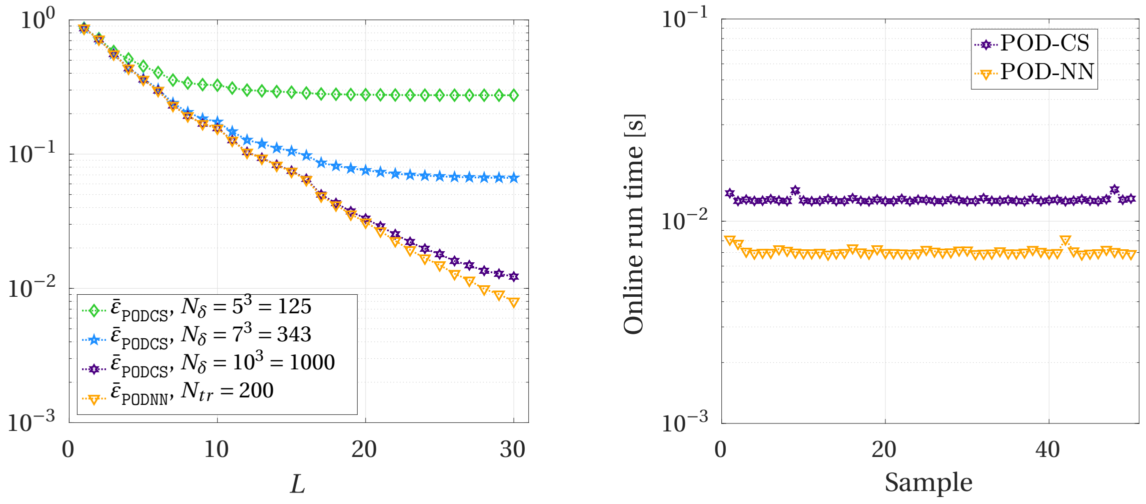

Figure 7.7. Average relative errors (*left*) and online run times (*right*) on Ξ_{te} for the POD-CS and the POD-NN methods applied to problem (7.5). For the latter, the results refer to an MLP equipped with $H_1 = H_2 = 35$ neurons per hidden layer.

For the Poisson problem (7.5), we report in the left plot of Fig. 7.7 the relative errors (averaged on Ξ_{te}) yielded by both the POD-CS and the POD-NN methods. For the former, we provide the results obtained on tensor-product grids consisting of N_δ interpolation points, with $N_\delta \in \{5^3, 7^3, 10^3\}$. For the latter, $H_1 = H_2 = 35$ neurons per hidden layer and $N_{tr} = 200$ training patterns have been used. Although the online performance of the two procedures are basically the same, as shown by the second plot in Fig. 7.7, we observe that the level of predictive accuracy enabled by the POD-NN method can be attained or at least approached by cubic spline interpolation only when this relies on $N_\delta = 1000$ samples. In fact, as mentioned in the Introduction, a standard interpolation technique may require a large number of samples, thus snapshots, to be able to enforce the constraints characterizing the nonlinear manifolds which the reduced bases typically belong to [1]. Hence, although this approach provides a valuable alternative for paremetrized problems with a few parameters, it may be unfeasible in real-life applications involving hundreads of parameters. Conversely, the secret hope behind the choice of a neural network-based regression is that the amount of required snapshots properly scales with the dimension of the parameter space. This would justify the overheads due to the training phase.

7.3. *The lid-driven cavity problem*

In this section, we are concerned with the numerical simulation of a viscous flow within a parallelogram-shaped cavity, illustrated in Fig. 7.8 (*left*). The geometry of the domain is affected by three parameters: $\mu_1 \in [1, 2]$ and $\mu_2 \in [1, 2]$ define the length of the horizontal and slanting (possibly vertical) edges, respectively, whereas $\mu_3 \in \left[\pi/6, 5\pi/6\right]$ denotes the angle between the oblique sides and the positive $\tilde{x}$-semiaxis. The Dirichlet boundary conditions enforced on the velocity field, graphically represented in Fig. 7.8 (*center*), are such that the flow is driven by a unit horizontal velocity at the top boundary [50]. For this reason, this benchmark is typically referred to as the *lid-driven cavity* problem. In addition, to retain the uniqueness of the solution, we fix the pressure at the lower-left corner [17]. Therefore, to properly resolve the steep velocity gradient near the upper boundary and the pressure singularities at the top corners, the computational mesh Ω_h (Fig. **??**, *right*) is refined in the upper part of the domain.

For the Navier-Stokes equations, a suitable choice of the FE spaces is crucial to fulfill the well-known *inf-sup* stability condition [54]. At this regard, a common and effective choice consists in using quadratic finite elements for the components of the velocity field and linear finite elements for the pressure, leading to the so-called $\mathbb{P}^2 - \mathbb{P}^1$ (or Taylor-Hood) FE discretization [50]. Figure 7.9 shows the velocity streamlines (*top*) and the pressure distribution (*bottom*) obtained through the resulting FE method for, from the left to the right, $\boldsymbol{\mu} = \left(1, 2/\sqrt{3}, 2\pi/3\right)$, $\boldsymbol{\mu} = \left(1, 1, \pi/2\right)$ or $\boldsymbol{\mu} = \left(1, 2/\sqrt{3}, \pi/6\right)$. Observe how the moving lid induces a large velocity gradient close to the top boundary, while it only slightly affects the fluid in the lower part of the cavity. In turn, this gives rising to two vortices, whose extent highly depends on the shape of the domain, or, equivalently, $\boldsymbol{\mu}$. Conversely, the pressure field does not undergo remarkable alterations across the parameter space. For all the configurations, a low-pressure region takes place at the upper-left corner of the domain and in the center of the

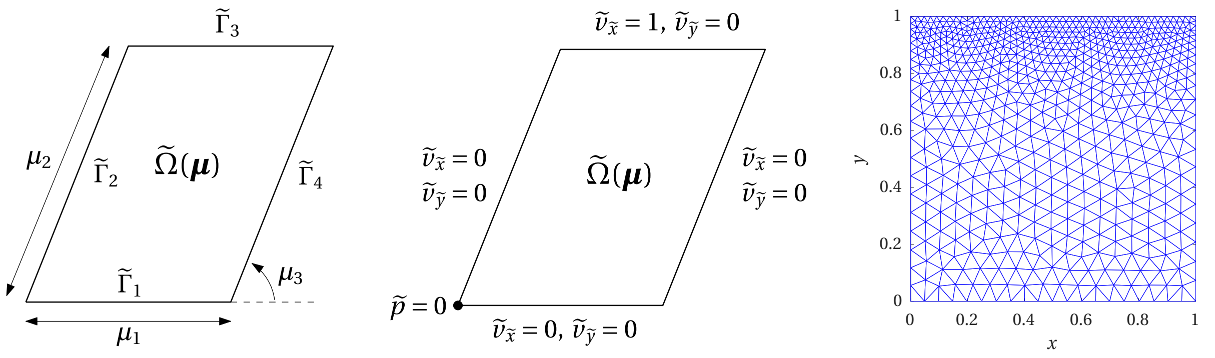
$\widetilde{\Gamma}_3$
μ_2
$\widetilde{\Gamma}_2$
$\widetilde{\Omega}(\boldsymbol{\mu})$
$\widetilde{\Gamma}_4$
$\widetilde{\Gamma}_1$
μ_3
μ_1
$\widetilde{v}_{\widetilde{x}} = 1,\ \widetilde{v}_{\widetilde{y}} = 0$
$\widetilde{v}_{\widetilde{x}} = 0$
$\widetilde{v}_{\widetilde{y}} = 0$
$\widetilde{p} = 0$
$\widetilde{v}_{\widetilde{x}} = 0,\ \widetilde{v}_{\widetilde{y}} = 0$
x
y

Figure 7.8. Computational domain (*left*), enforced velocity at the boundaries (*center*) and computational mesh Ω_h (*right*) for the lid-driven cavity problem for the uncompressible Navier-Stokes equations.

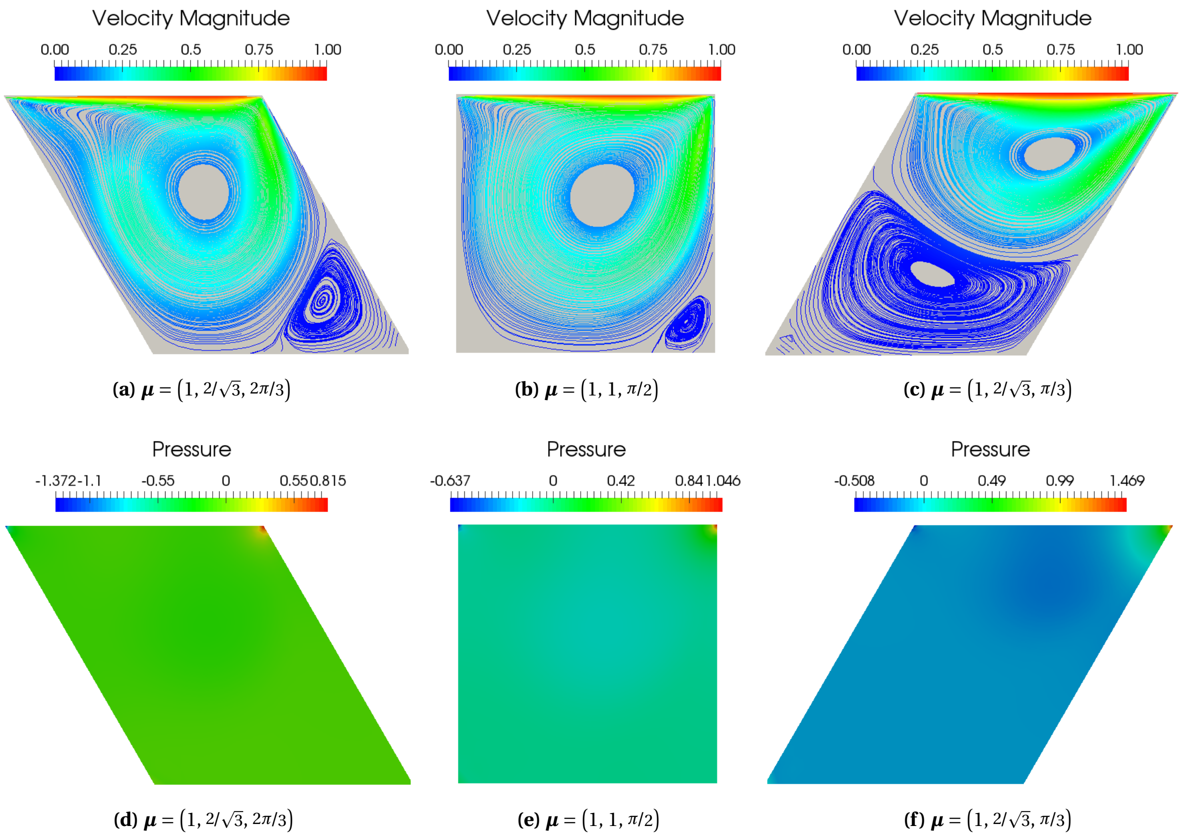

Figure 7.9. Velocity streamlines (*top*) and pressure distribution (*bottom*) for the lid-driven cavity problem, computed through the FE method. Three different parameter values are considered; for all configurations, the Reynold's number is 400.

major vortex (although it may be not clearly visible). Instead, the upper-right corner represents a stagnation point for the $\widetilde{x}$-velocity, and so therein the pressure assumes larger values than in the rest of the cavity [17].

All the results presented in Fig. 7.9 refer to a Reynold's number of 400. The Reynold's number is an adimensional group, defined as the ratio between the inertia and the viscous (or friction) force. For the specific problem at hand, it reads:

$$Re = \frac{\max\{\mu_1, \mu_2\}}{\nu(\boldsymbol{\mu})},$$

with $\nu = \nu(\boldsymbol{\mu})$ being the dynamic viscosity of the fluid. In our analyses, $\nu(\boldsymbol{\mu})$ is adapted as the geometry varies so that the Reynold's number is either 200 or 400.

Regarding the reduced-order modeling of the parametrized problem of interest, we slightly distance ourselves from the general workflow depicted in Sections 5 and 6. Indeed, for the Navier-Stokes equations is convenient to construct two separate reduced spaces [2, 12, 53]: $X_{\mathtt{rb}}$, with dimension $L_{\boldsymbol{v}}$, for the velocity field and $Q_{\mathtt{rb}}$, with dimension L_p, for the pressure distribution, respectively represented by the matrices

$$\mathbb{V}_{\boldsymbol{v}} = \left[\boldsymbol{\psi}_1^{\boldsymbol{v}} \,|\, \dots \,|\, \boldsymbol{\psi}_{L_{\boldsymbol{v}}}^{\boldsymbol{v}}\right] \in \mathbb{R}^{M_{\boldsymbol{v}} \times L_{\boldsymbol{v}}} \quad \text{and} \quad \mathbb{V}_p = \left[\boldsymbol{\psi}_1^{p} \,|\, \dots \,|\, \boldsymbol{\psi}_{L_p}^{p}\right] \in \mathbb{R}^{M_p \times L_p},$$

with $M_{\boldsymbol{v}}$ (respectively, M_p) the size of the FE velocity (resp., pressure) space.

Actually, although the underpinning finite element solver has been designed to fulfill the inf-sup condition, thus ensuring the stability of the scheme, when dealing with incompressible flows this property may not be automatically inherited by the POD-Galerkin reduced-order solver, which as a result may show severe instabilities [8]. Indeed, one has to carefully choose the reduced velocity space $X_{\mathtt{rb}}$ so to meet an equivalent of the inf-sup condition at the reduced level. To this end, in our simulations we resort to a *supremizer enrichment* of $X_{\mathtt{rb}}$, as proposed in [2] (to which we refer the readers which are interested in the rational and details of this approach). At each pressure snapshot $\mathbf{p}_h\big(\boldsymbol{\mu}^{(n)}\big) \in \mathbb{R}^{M_p}$, $n = 1, \dots, N$, we associate the *supremizer solution* $\mathbf{s}_h\big(\boldsymbol{\mu}^{(n)}\big) \in \mathbb{R}^{M_{\boldsymbol{v}}}$, defined as the solution to a linear system of the form

$$\mathbb{A}\, \mathbf{s}_h\big(\boldsymbol{\mu}^{(n)}\big) = \mathbb{B}\big(\boldsymbol{\mu}^{(n)}\big)\, \mathbf{p}_h\big(\boldsymbol{\mu}^{(n)}\big),$$

with $\mathbb{A} \in \mathbb{R}^{M_{\boldsymbol{v}} \times M_{\boldsymbol{v}}}$ and $\mathbb{B}\big(\boldsymbol{\mu}^{(n)}\big) \in \mathbb{R}^{M_{\boldsymbol{v}} \times M_p}$. Letting $\mathbb{V}_{\boldsymbol{s}} = \left[\boldsymbol{\psi}_1^{\boldsymbol{s}} \,|\, \dots \,|\, \boldsymbol{\psi}_{L_{\boldsymbol{s}}}^{\boldsymbol{s}}\right] \in \mathbb{R}^{M_{\boldsymbol{v}} \times L_{\boldsymbol{s}}}$ be the POD basis of rank $L_{\boldsymbol{s}}$ extracted from the ensemble of snapshots $\{\mathbf{s}\big(\boldsymbol{\mu}^{(1)}\big), \dots, \mathbf{s}\big(\boldsymbol{\mu}^{(N)}\big)\}$, the POD-G approximation of the velocity field is then sought in the form

$$\bar{\mathbf{v}}_L(\boldsymbol{\mu}) = \overline{\mathbb{V}}_{\boldsymbol{v}}\, \bar{\mathbf{v}}_{\mathtt{rb}}(\boldsymbol{\mu}) = \sum_{i=1}^{L_{\boldsymbol{v}}} v_{\mathtt{rb}}^{(i)} \boldsymbol{\psi}_i^{\boldsymbol{v}} + \sum_{i=1}^{L_{\boldsymbol{s}}} s_{\mathtt{rb}}^{(i)} \boldsymbol{\psi}_i^{\boldsymbol{s}},$$

where

$$\overline{\mathbb{V}}_{\boldsymbol{v}} = [\mathbb{V}_{\boldsymbol{v}}\ \mathbb{V}_{\boldsymbol{s}}] \in \mathbb{R}^{M_{\boldsymbol{v}} \times (L_{\boldsymbol{v}} + L_{\boldsymbol{s}})} \quad \text{and} \quad \bar{\mathbf{v}}_{\mathtt{rb}}(\boldsymbol{\mu}) = \begin{bmatrix} \mathbf{v}_{\mathtt{rb}}(\boldsymbol{\mu}) \\ \mathbf{s}_{\mathtt{rb}}(\boldsymbol{\mu}) \end{bmatrix} \in \mathbb{R}^{L_{\boldsymbol{v}} + L_{\boldsymbol{s}}}.$$

In [2], several numerical evidences suggest that a proper value for $L_{\boldsymbol{s}}$ should lay in between $L_p/2$ and L_p. In our simulations, we set $L_{\boldsymbol{s}} = L_p = L_{\boldsymbol{v}}$, leading to a stable reduced (nonlinear) system in $L = 3\, L_{\boldsymbol{v}}$ unknowns.

Concerning the POD-NN procedure, for any $\boldsymbol{\mu} \in \mathscr{P}$, reduced-order discretizations $\mathbf{v}_{L_{\boldsymbol{v}}}^{\mathtt{NN}}(\boldsymbol{\mu})$ and $\mathbf{p}_{L_p}^{\mathtt{NN}}(\boldsymbol{\mu})$ of $\boldsymbol{v}(\boldsymbol{\mu})$ and $p(\boldsymbol{\mu})$, respectively, are sought in the form

$$\mathbf{v}_{L_{\boldsymbol{v}}}^{\mathtt{NN}}(\boldsymbol{\mu}) = \mathbb{V}_{\boldsymbol{v}}\, \mathbf{v}_{\mathtt{rb}}^{\mathtt{NN}}(\boldsymbol{\mu}) \quad \text{and} \quad \mathbf{p}_{L_p}^{\mathtt{NN}}(\boldsymbol{\mu}) = \mathbb{V}_p\, \mathbf{p}_{\mathtt{rb}}^{\mathtt{NN}}(\boldsymbol{\mu}).$$

Here, $\mathbf{v}_{\mathtt{rb}}^{\mathtt{NN}}(\boldsymbol{\mu})$ and $\mathbf{p}_{\mathtt{rb}}^{\mathtt{NN}}(\boldsymbol{\mu})$ denote the output vectors provided by two *distinct* multi-layer perceptrons, respectively trained with the ensemble of input-output patterns

$$\big\{\boldsymbol{\mu}^{(i)}, \mathbb{V}_{\boldsymbol{v}}^T \mathbf{v}_h\big(\boldsymbol{\mu}^{(i)}\big)\big\}_{i=1}^{N_{tr}} \quad \text{and} \quad \big\{\boldsymbol{\mu}^{(i)}, \mathbb{V}_p^T \mathbf{p}_h\big(\boldsymbol{\mu}^{(i)}\big)\big\}_{i=1}^{N_{tr}}.$$

At this regard, let us point out two important remarks.

(i) The supremizer solutions are not involved (either directly or indirectly) in the POD-NN framework. Indeed, they ensure the overall stability of the POD-Galerkin procedure, but they do not power-up the accuracy of the method, and so they can be disregarded whenever stability is not an issue.

(ii) The routine outlined in Section 6, aiming at finding an optimal network configuration, is applied *separately* to the

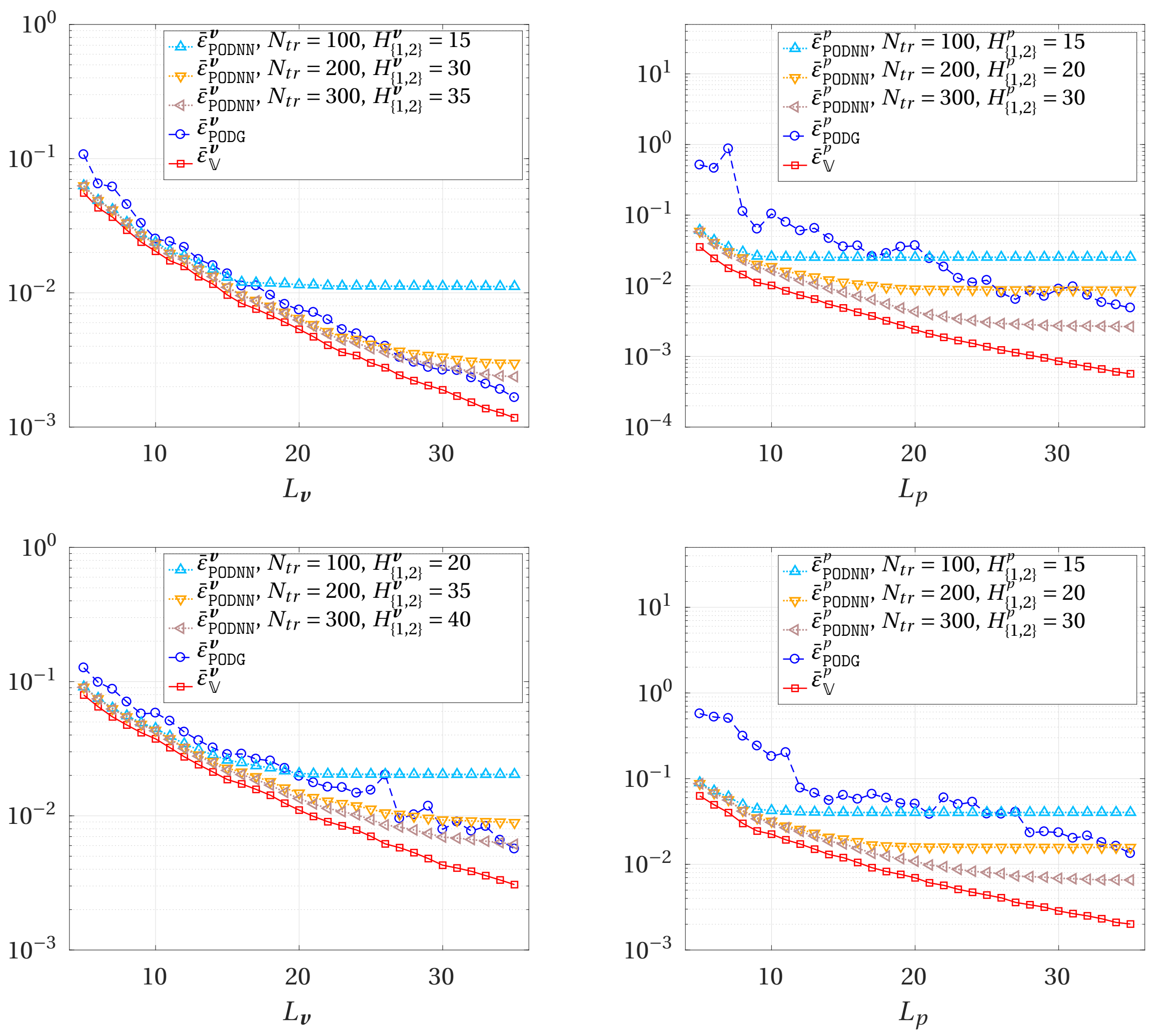

Figure 7.10. Velocity (*left*) and pressure (*right*) error analysis for the POD-G and POD-NN methods applied to the lid-driven cavity problem with $Re = 200$ (*top*) and $Re = 400$ (*bottom*).

perceptrons designated to predict the velocity field and to the perceptrons required to approximate the pressure distribution. As a result, once the offline phase of the POD-NN method is completed, we may end up with two completely different networks, equipped with $H_1^{\boldsymbol{v}} = H_2^{\boldsymbol{v}}$ and $H_1^{p} = H_2^{p}$ computing units per hidden layer, respectively.

Figure 7.10 reports the error committed by both RB procedures when approximating the velocity field (*left*) and the pressure distribution (*right*) by means of $L_{\boldsymbol{v}}$ velocity modes, L_p pressure modes and, exclusively for the POD-Galerkin method, $L_{\boldsymbol{s}}$ supremizer modes, with $5 \leq L_{\boldsymbol{v}} = L_{\boldsymbol{s}} = L_p \leq 35$. The plots on the top refer to a Reynold's number of 200, the ones on the bottom to a Reynold's number of 400. Please note that for clarity of illustration, the symbols denoting the projection, POD-G and POD-NN errors have been decorated with a superscript (either $\boldsymbol{v}$ or p) recalling the state variable they refer to.

While the error yielded on the velocity field shows an almost perfect exponential decay with the number of POD modes included in the RB model, the POD-G method faces difficulties in providing a correct recovery of the pressure, already for $Re = 200$. Indeed, the corresponding error curve may not be monotone, and generally lays at least one order of magnitude above the projection error. On the contrary, the POD-NN method attains a satisfactory predictive accuracy. Particularly, the advantages of resorting to a neural network-based nonlinear regression coupled with a POD procedure are evident when the approximation is built upon a few basis functions, say $L_p < 20$. However, even for $L_p = 35$ (i.e., the dimension of the

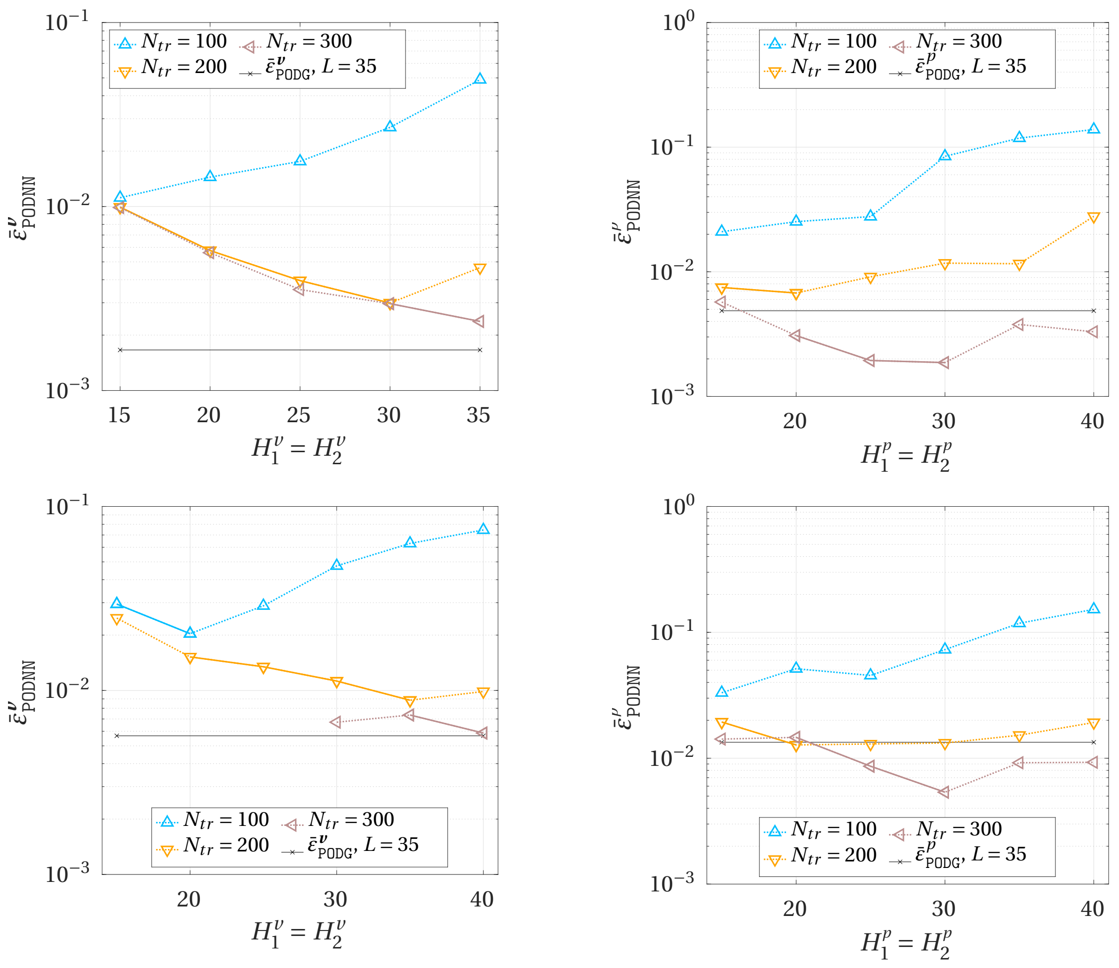

Figure 7.11. Convergence analysis with respect to the number of hidden neurons and training samples used within the POD-NN procedure to approximate the velocity field (*left*) and the pressure distribution (*right*) by means of 35 modal functions. The Reynold's number is either 200 (*top*) or 400 (*bottom*).

largest basis tested in our experiments), the POD-NN error is smaller than the POD-G one. Moreover, the proposed routine recommends to use fewer neurons to predict the POD coefficients for the pressure than for the velocity, thus resulting in a lighter perceptron.

This is confirmed also by Fig. 7.11, which provides a sensitivity analysis of the predictive accuracy featured by the POD-NN method with respect the amount of neurons and training samples used. Observe that for the pressure (*right*), employing more than 30 neurons within each hidden layer is counter-productive, both for $Re = 200$ (*top*) and $Re = 400$ (*bottom*). This assertion agrees with the peculiar role played by the pressure in the parametrized lid-driven cavity problem, with similar patterns featured across the entire parameter domain.

On the contrary, we have seen that the velocity field presents more complex dynamics, highly varying with the domain configuration. As a result, an optimal approximation of the velocity is obtained for the maximum values of $H_i^{\boldsymbol{v}}$, $i = 1, 2$, and N_{tr} tested, that is, $H_1^{\boldsymbol{v}} = H_2^{\boldsymbol{v}} = 35$ and $N_{tr} = 300$ for $Re = 200$, $H_1^{\boldsymbol{v}} = H_2^{\boldsymbol{v}} = 40$ and $N_{tr} = 300$ for $Re = 400$. Moreover, we may not be able to exactly attain the same precision enabled by the standard POD-Galerkin procedure, although the results are quite similar. However, this (slight) loss of accuracy is offset by a (great) reduction in the online run time: the POD-NN method takes around 2/100 of seconds per query, against the average 40 seconds required by the POD-G method; see Fig. 7.12. As for the test cases for the Poisson problem, this comes at the cost of a longer offline phase. In fact, the research and training of sufficiently accurate perceptrons lasted about 4.5 hours here.

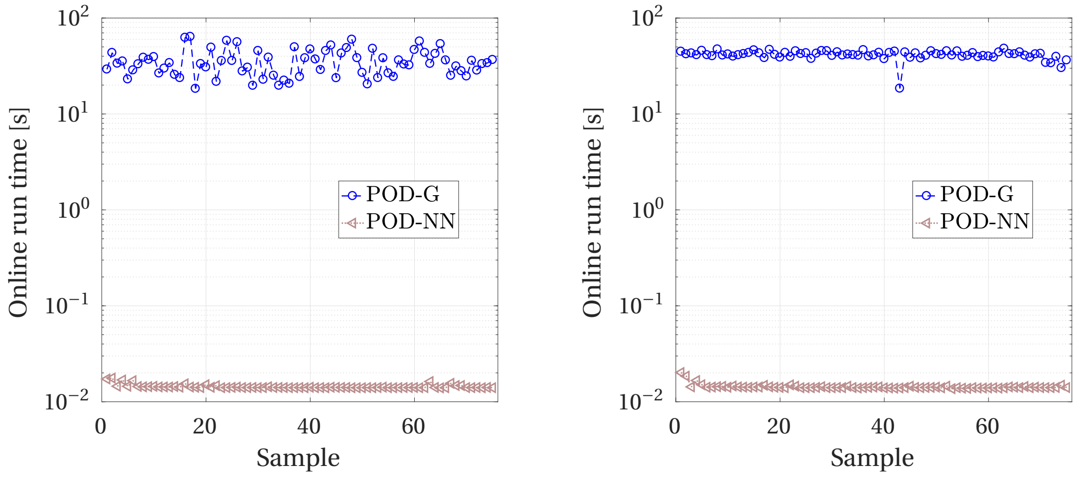

Figure 7.12. Online run times for the POD-G and the POD-NN method applied to the lid-driven cavity problem with $Re = 200$ (*left*) and $Re = 400$ (*right*). $N_{te} = 75$ test configurations are considered. For the POD-NN method, the reported times include the (sequential) evaluation of both neural networks for the velocity and pressure field.

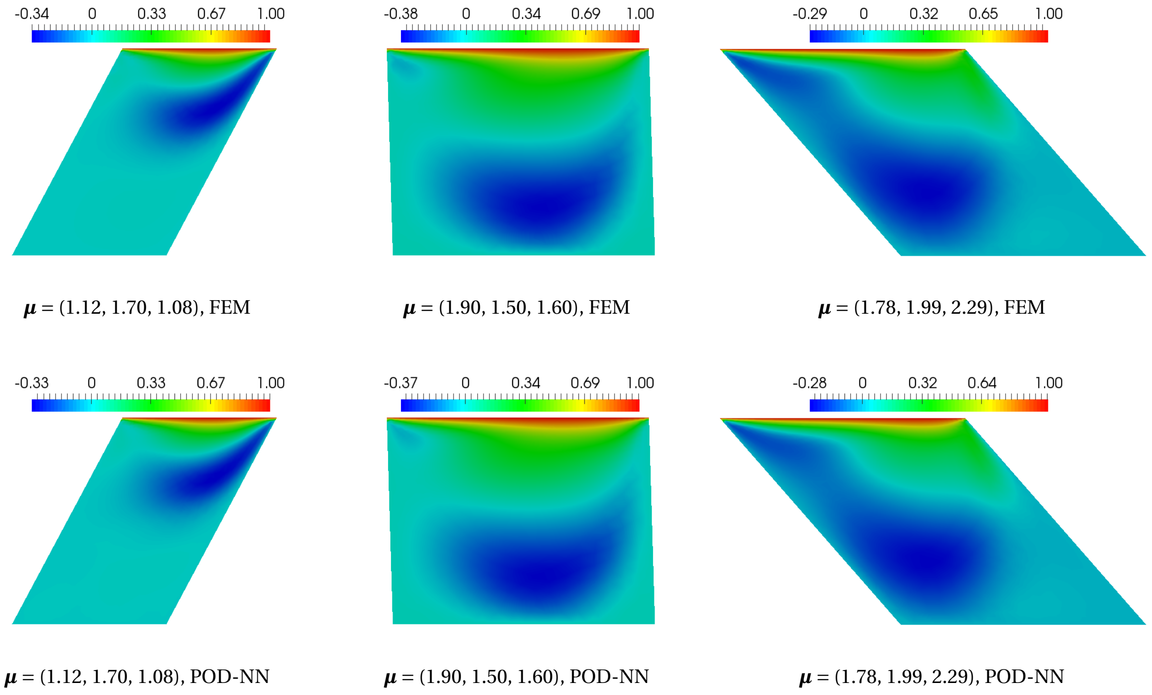

Figure 7.13. $\tilde{x}$-velocity contour at three parameter values, as computed through the FE (*top row*) and POD-NN (*bottom row*) method. For each configuration, the Reynold's number is 400.

Another numerical evidence of the predictive accuracy of the proposed POD-NN RB method is provided in Fig. 7.13, showing the contour plots for the $\tilde{x}$-velocity computed through the FE (*top row*) and the POD-NN (*bottom row*) scheme. Three different configurations, corresponding to as many input vectors, are considered; the Reynold's number is fixed to 400. We can appreciate the good agreement between the solutions given by the full-order and the reduced-order methods.

Lastly, Fig. 7.14 compares the streamlines obtained through the direct method (*top*) and the proposed reduced basis approach (*bottom*) over the three configurations previously considered. Streamlines provide an interesting test bed, as minor variations in velocity contours may lead to substantial differences in the streamlines [12]. However, we observe

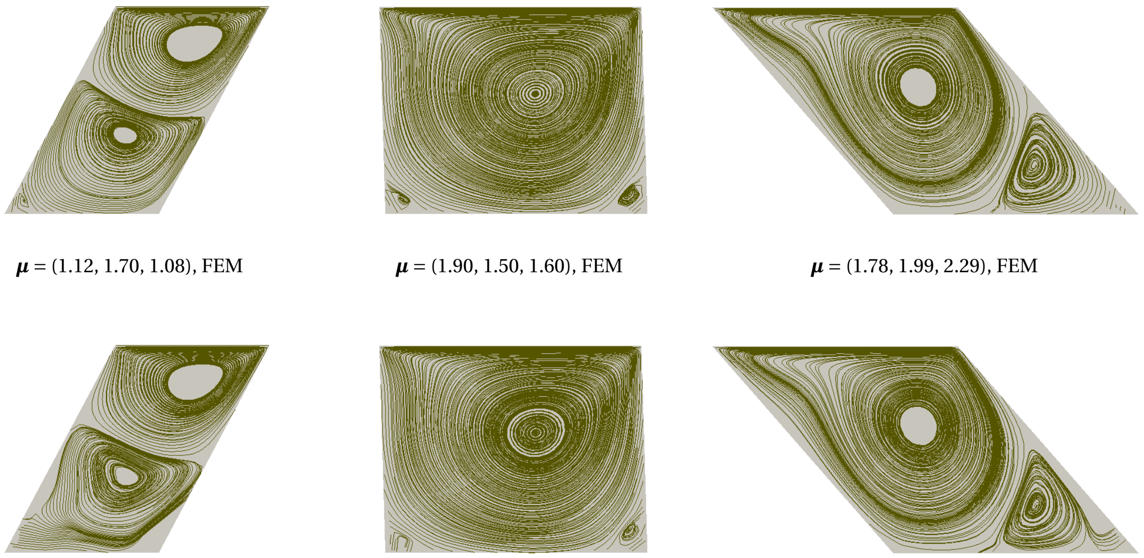

$\boldsymbol{\mu} = (1.12, 1.70, 1.08)$, FEM $\boldsymbol{\mu} = (1.90, 1.50, 1.60)$, FEM $\boldsymbol{\mu} = (1.78, 1.99, 2.29)$, FEM

$\boldsymbol{\mu} = (1.12, 1.70, 1.08)$, POD-NN $\boldsymbol{\mu} = (1.90, 1.50, 1.60)$, POD-NN $\boldsymbol{\mu} = (1.78, 1.99, 2.29)$, POD-NN

Figure 7.14. Streamlines at three parameter values, as computed through the FE (*top row*) and POD-NN (*bottom row*) method. For each configuration, the Reynold's number is 400.

a good agreement between the two methods. In particular, in the second example, the POD-NN method is still able to detect the two micro recirculation zones at the lower corners of the domain. Whereas, the method partially fails in properly describing the velocity field at the bottom-left corner in the first configuration and at the bottom-right corner in the last configuration. However, these are dead zones, so we can safely disregard these little imprecisions.

8. Conclusion

In this work, we have developed a non-intrusive RB method (referred to as POD-NN) for parametrized time-independent differential problems. The method extracts a reduced basis from a collection of snapshots through a POD procedure and employs multi-layer perceptrons to approximate the coefficients of the reduced model. By exploiting the fundamental results by Cybenko (see Subsection 2.2), we can limit ourselves to perceptrons endowed with two hidden layers. The identification of the optimal number of inner neurons and the minimum amount of training samples which prevents overfitting is performed at the offline stage through an automatic routine, relying upon the latin hypercube sampling and the Levenberg-Marquardt training algorithm. On the one hand, this guarantees a complete decoupling between the offline and the online phase, with the latter which entails a computational cost independent of the dimension of the full-order model. On the other hand, this unavoidably extends the offline stage with respect to a standard projection-based RB procedure, making the POD-NN method practically convenient only when the underlying PDE has to be solved for many parameter values (many-query context). At this regard, the method would surely benefit from a GPU-powered implementation, enabling a high parallelization of the code.

The POD-NN method has been successfully tested on the nonlinear Poisson equation in one and two spatial dimensions, and on two-dimensional cavity viscous flows, modeled through the steady uncompressible Navier-Stokes equations. In particular, the proposed RB strategy enabled the same predictive accuracy provided by the POD-Galerkin method while reducing by two or even three order of magnitudes the CPU time required to process an online query.

All the test cases considered in our numerical studies involved three parameters, affecting either physical or geometrical factors of the differential problem. The extension of the POD-NN method to time-dependent problems depending on many parameters is left as future work. In this respect, the secret hope behind a neural network-based interpolation is that the number of training samples, thus snapshots, required to achieve a given level of accuracy properly scales with the dimension of the parameter space. In fact, as observed in Subsection 7.2, this represents the major weak point of traditional interpolation techniques.

Lastly, let us point out that although in this work we used POD to recover a reduced space, this choice is not binding, and a greedy approach may also be pursued.

References

[1] Amsallem., D. (2010). *Interpolation on manifolds of CFD-based fluid and finite element-based structural reduced-order models for on-line aeroelastic predictions.* Doctoral dissertation, Department of Aeronautics and Astronautics, Stanford University.

[2] Ballarin, F., Manzoni, A., Quarteroni, A., Rozza, G. (2014). *Supremizer stabilization of POD-Galerkin approximation of parametrized Navier-Stokes equations.* MATHICSE Technical Report, École Polytechnique Fédérale de Lausanne.

[3] Barrault, M., Maday, Y., Nguyen, N. C., Patera, A. T. (2004). *An 'empirical interpolation' method: Application to efficient reduced-basis discretization of partial differential equations.* Comptes Rendus Mathematique, 339(9):667-672.

[4] Barthelmann, V., Novak, E., Ritter, K. (2000). *High-dimensional polynomial interpolation on sparse grids.* Advances in Computational Mathematics, 12(4):273-288.

[5] Bendsøe, M. P., Sigmund, O. (2004). *Topology optimization: Theory, methods and applications.* Heidelberg, DE: Springer Science & Business Media.

[6] Brown, P. F., Pietra, V. J. D., Pietra, S. A. D., Mercer, R. L. (1993). *The mathematics of statistical machine translation: Parameter estimation.* Computational linguistics, 19(2):263-311.

[7] Buffa, A., Maday, Y., Patera, A. T., Prud'Homme, C., Turinici, G. (2012). *A priori convergence of the greedy algorithm for the parametrized reduced basis method.* ESAIM: Mathematical Modelling and Numerical Analysis, 46:595-603.

[8] Burkardt, J., Gunzburger, M., Lee, H. C. (2006). *POD and CVT-based reduced-order modeling of Navier-Stokes flows.* Computer Methods in Applied Mechanics and Egninnering, 196:337-355.

[9] Casenave, F., Ern, A., Lelièvre, T. (2015). *A nonintrusive reduced basis method applied to aeroacoustic simulations.* Advances in Computational Mathematics, 41:961-986.

[10] Chaturantabut, S., Sorensen, D. C. (2010). *Nonlinear model reduction via discrete empirical interpolation.* SIAM Journal on Scientific Computing, 32(5):2737-2764.

[11] Caloz, G., Rappaz, J. (1997). *Numerical analysis and bifurcation problems.* Handbook of numerical analysis, 5(2):487-637.

[12] Chen, W., Hesthaven, J. S., Junqiang, B., Yang, Z., Tihao, Y. (2017). *A greedy non-intrusive reduced order model for fluid dynamics.* Submitted to American Institute of Aeronautics and Astronautics.

[13] Cybenko, G. (1988). *Continuous valued neural networks with two hidden layers are sufficient.* Technical Report, Department of Computer Science, Tufts University.

[14] Cybenko, G. (1989). *Approximation by superpositions of a sigmoidal function.* Mathematics of Control, Signals, and Systems, 2(4):303–314.

[15] De Boor, C. (1978). *A practical guide to splines.* New York, NY: Springer-Verlag.

[16] Deparis, S. (2008). *Reduced basis error bound computation of parameter-dependent Navier-Stokes equations by the natural norm approach.* SIAM Journal of Numerical Analysis, 46(4):2039-2067.

[17] Dhondt, G. (2014). *CalculiX CrunchiX user's manual.* Available at `http://web.mit.edu/calculix_v2.7/CalculiX/ccx_2.7/doc/ccx/node1.html`.

[18] Eckart, C., Young, G. (1936). *The approximation of one matrix by another of lower rank.* Psychometrika, 1:211-218.

[19] Eftang, J. L. (2008). *Reduced basis methods for partial differential equations.* Master thesis, Department of Mathematical Sciences, Norwegian University of Science and Technology.

[20] Elman, H. C., Silvester, D. J., Wathen, A. (2004). *Finite elements and fast iterative solvers with applications in incompressible fluid dynamics.* New York, NY: Oxford University Press.

[21] Fahlman, S. E. (1988). *An empirical study of learning speed in back-propagation networks.* Technical Report CMU-CS-88-162, CMU.

[22] Gill, P. E., Murray, W., Wright, M. H. (1981). *Practical optimization.* Academic Press.

[23] Hagan, M. T., Menhaj, M. B. (1994). *Training feedforward networks with the Marquardt algorithm.* IEEE Transactions on Neural Networks, 5(6):989-993.

[24] Hagan, M. T., Demuth, H. B., Beale, M. H., De Jesús, O. (2014). *Neural Network Design, 2nd Edition.* Retrieved from `http://hagan.okstate.edu/NNDesign.pdf`.

[25] Hassdonk, B. (2013). *Model reduction for parametric and nonlinear problems via reduced basis and kernel methods.* CEES Computational Geoscience Seminar, Stanford University.

[26] Haykin, S. (2004). *Neural Networks: A comprehensive foundation.* Upper Saddle River, NJ: Prentice Hall.

[27] Hebb, D. O. (1949). *The organization of behaviour: A neuropsychological theory.* New York, NY: John Wiley & Sons.

[28] Liang, Y. C., Lee, H. P., Lim, S. P., Lin, W. Z., Lee, K. H., Wu, C. G. (2002) *Proper Orthogonal Decomposition and its applications - Part I: Theory.* Journal of Sound and Vibration, 252(3):527-544.

[29] Hassibi, B., Stork, D. G. (1993). *Second order derivatives for network pruning: Optimal Brain Surgeon.* Advances in neural information processing systems, 164-171.

[30] Hesthaven, J. S., Stamn, B., Rozza, G. (2016). *Certified reduced basis methods for parametrized partial differential equations.* New York, NY: Springer.

[31] Hesthaven, J. S., Stamn, B., Zhang, S. (2014). *Efficienty greedy algorithms for high-dimensional parameter spaces with applications to empirical interpolation and reduced basis methods.* ESAIM: Mathematical Modelling and Numerical Analysis, 48(1):259-283.

[32] Hopfield, J. J. (1982). *Neural networks and physical systems with emergent collective computational abilities.* Proceedings of the National Acadamedy Science, 79:2554-2558.

[33] Imam, R. L. (2008). *Latin hypercube sampling.* Encyclopedia of Quantitative Risk Analysis and Assessment.

[34] Jaggli, C., Iapichino, L., Rozza, G. (2014). *An improvement on geometrical parametrizations by transfinite maps.* Comptes Rendus de l'Académie des Sciences Paris, Series I, 352:263-268.

[35] Kaelbling, L. P., Littman, M. L., Moore, A. W. (1996). *Reinforcement Learning: A Survey.* Journal of Artificial Intelligence Reserch, 4:237-285.

[36] Kohavi, R. (1995). *A study of cross-validation and bootstrap for accuracy estimation and model selection.* Proceedings of the 40^{th} International Joint Conference on Artificial Intelligence, 2(12):1137-1143.

[37] Kohonen, T. (1998). *The self-organizing map.* Neurocomputing, 21(1-3):1-6.

[38] Kriesel, D. (2007). *A Brief Introduction to Neural Networks.* Retrieved from `http://www.dkriesel.com/en/science/neural_networks`.

[39] Le Maître, O., Knio, O. M. (2010). *Spectral methods for uncertainty quantification with applications to computational fluid dynamics.* Berlin, DE: Springer Science & Business Media.

[40] Lee, E. B., Markus, L. (1967). *Foundations of optimal control theory.* New York, NY: John Wiley & Sons.

[41] Maday, Y. (2006) *Reduced basis method for the rapid and reliable solution of partial differential equations.* Proceedings of the International Congress of Mathematicians, Madrid, Spain, 1255-1269.

[42] Marquardt, D. W. (1963). *An algorithm for least-squares estimation of nonlinear parameters*. Journal of the Society for Industrial and Applied Mathematics, 11(2):431-441.

[43] The MathWorks, Inc. (2016). *Machine learning challenges: Choosing the best model and avoiding overfitting*. Retrieved from `https://it.mathworks.com/campaigns/products/offer/common-machine-learning-challenges.html`.

[44] Mitchell, W., McClain, M. A. (2010). *A collection of 2D elliptic problems for testing adaptive algorithms*. NISTIR 7668.

[45] Manzoni, A., Negri, F. (2016). *Automatic reduction of PDEs defined on domains with variable shape*. MATHICSE technical report, École Polytechnique Fédérale de Lausanne.

[46] Møller, M. D. (1993). *A scaled conjugate gradient algorithm for fast supervised learning*. Neural Networks, 6:525-533.

[47] McClelland, J. L., Rumelhart, D. E. (1986). *Parallel Distributed Processing: Explorations in the Microstructure of Cognition*. Cambridge, UK: MIT Press.

[48] Nielsen, M. A. (2015). *Neural Networks and Deep Learning*. Determination Press.

[49] Negri, F., Manzoni, A., Amsallem, D. (2015). *Efficient model reduction of parametrized systems by matrix discrete empirical interpolation*. Journal of Computational Physics, 303:431-454.

[50] Persson, P. O. (2002). *Implementation of finite-element based Navier-Stokes solver*. Massachussets Institue of Technology.

[51] Prud'homme, C., Rovas, D. V., Veroy, K., Machiels, L., Maday, Y., Patera, A. T., Turinici, G. (2002). *Reliable real-time solution of parametrized partial differential equations: Reduced-basis output bound methods*. Journal of Fluids Engineering, 124(1):70-80.

[52] Quarteroni, A. (2010). *Numerical models for differential problems* (Vol. 2). New York, NY: Springer Science & Business Media.

[53] Quarteroni, A., Manzoni, A., Negri, F. (2015). *Reduced basis methods for partial differential equations: An introduction* (Vol. 92). New York, NY: Springer, 2015.

[54] Rannacher, R. (1999). *Finite element methods for the incompressible Navier-Stokes equations*. Lecture notes, Institute of Applied Mathematics, University of Heidelberg.

[55] Riedmiller, M., Braun, H. (1993). *A direct adaptive method for faster backpropagation learning: The rprop algorithm*. Neural Networks, IEEE International Conference on, 596-591.

[56] Rosenblatt, F. (1958). *The perceptron: A probabilistic model for information storage and organization in the brain*. Psychological Review, 65:386-408.

[57] Rudin, W. (1964). *Principles of mathematical analysis* (Vol. 3). New York, NY: McGraw-Hill.

[58] Schmidt, E. (1907). *Zur theorie der linearen und nichtlinearen integralgleichungen. I. Teil: Entwicklung willkürlicher funktionen nach systemen vorgeschriebener*. Mathematische Annalen, 63:433-476.

[59] Stergiou, C., Siganos, D. (2013). *Neural Networks*. Retrieved from `https://www.doc.ic.ac.uk/~nd/surprise_96/journal/vol4/cs11/report.html#Introductiontoneuralnetworks`.

[60] Volkwein, S. (2008). *Model reduction using proper orthogonal decomposition*. Lecture notes, Department of Mathematics, University of Konstanz.

[61] Widrow, B., Hoff, M. E. (1960). *Adaptive switching circuits*. Proceedings WESCON, 96-104.